MAPPING SPINACH YIELD USING UAV-BASED MULTISPECTRAL IMAGERY DATA

Xintong Jiang

Supervisor: Dr. Shangpeng Sun

Co-supervisor: Dr. Viacheslav Adamchuk

Department of Bioresource Engineering

McGill University, Montreal

July 2023

A thesis submitted to McGill University in partial fulfillment of the requirements of the degree of Master of Science

Table of Contents

TABLE OF CONTENTS **2**

TABLE OF FIGURES **4**

TABLE OF TABLES **5**

LIST OF ACRONYMS **5**

ABSTRACT **7**

RÉSUMÉ **8**

ACKNOWLEDGMENTS **9**

CONTRIBUTION OF AUTHORS **10**

CHAPTER 1. INTRODUCTION **11**

1.1 BACKGROUND 11

1.2 OBJECTIVES 12

CHAPTER 2. LITERATURE REVIEW **14**

2.1 REMOTE SENSING 14

2.2 VEGETATION INDEX 15

2.3 CROP YIELD PREDICTION AND MAPPING 17

2.4 STATISTICAL CONSIDERATION 18

2.4.1. Multiple Linear Regression *18*

2.4.2 Variable Selection *19*

2.4.3. Prediction Performance Evaluation *20*

2.4.4. Influential Observations and Outliers *21*

CHAPTER 3. MATERIALS AND METHODS **23**

3.1 DATA COLLECTION 23

3.2 IMAGE PROCESSING 29

3.2.1 Orthomosaic Rotation *29*

3.2.2 Bed Boundary Detection *32*

3.3 ESTIMATION OF VEGETATION INDICES 35

3.4 CHOICE OF VARIABLES AND SAMPLE SIZE 37

3.5 MODEL SELECTION AND VALIDATION 37

CHAPTER 4. RESULTS AND DISCUSSION **40**

4.1 IMAGE PROCESSING 40
4.2 CORRELATIONS AND MODEL FITTING 41
4.3 ASSUMPTION VALIDATION 45
4.4 MODEL VALIDATION 48
4.5 YIELD MAPPING 51
4.6 DISCUSSION 53
CHAPTER 5. SUMMARY AND CONCLUSIONS 58
REFERENCES 59

Table of Figures

Figure 1. The data collection and processing protocol during the 2021 and 2022 growing seasons 23

Figure 2. The first round of data collection in 2021 produced a testing dataset of RGB and multispectral imagery of a spinach field in its early, middle, and late stages of growth. 26

Figure 3. Fields CA303 and CA304 on the day of UAV imagery collection, July 15, 2022..... 28

Figure 4. The algorithm to conduct the orthomosaic map rotation..... 31

Figure 5. An example area selected as the ROI in the UAV orthomosaic of a spinach field in its early growth stage in July 2021 to determine the angle of rotation..... 32

Figure 6. The algorithm to conduct vertical boundary delineation..... 34

Figure 7. The buffer created for a manually harvested sampling area for the training dataset 35

Figure 8. Representative results derived using the proposed image processing workflow 41

Figure 9. The correlation matrices between manually harvested biomass, canopy temperature and the 12 selected VIs of the training dataset 44

Figure 10. Assumptions verification of the model fitted with all observations..... 46

Figure 11. Assumptions verification of the model fitted without the 5 identified influential observations..... 47

Figure 12. Comparing the leftovers from manual-harvested and machine-harvested spinach bed..... 49

Figure 13. The ground truth yields versus the scaled predicted yield 49

Figure 14. VF and ExG of the training dataset and the validation dataset 51

Figure 15. Predicted yield map for unit areas in fields CA303 and CA304 (unit area length = 1 m)..... 52

Table of Tables

Table 1. Dataset Summary 24
Table 2. Potential VIs for spinach yield prediction 36
Table 3. Comparison of candidate models 43

List of Acronyms

AIC – Akaike Information Criterion

BIC – Bayesian Information Criterion

CI-RE – Chlorophyll Index - Red-Edge

CIVE – Color Index of Vegetation

CVI – Chlorophyll Vegetation Index

EVI – Enhanced Vegetation Index

ExG – Excess Green Index

GLI – Green Leaf Index

GNDVI – Green Normalized Difference Vegetation Index

GNSS – Global Navigation Satellite System

GSD – Ground Sample Distance

LASSO – Least Absolute Shrinkage and Selection Operator

MAE – Mean Absolute Error

MAPE – Mean Absolute Percentage Error

MGRVI – Modified Green Red Vegetation Index

ML – Machine Learning

MODIS – Moderate Resolution Imaging Spectroradiometer

NDRE – Normalized Difference Red Edge Index

NDVI – Normalized Difference Vegetation Index

NIR – Near Infrared

NLI – Nonlinear Vegetation Index

NN – Neural Network

OSAVI – Optimized Soil Adjusted Vegetation Index

PA – Precision Agriculture

R^2 – Coefficient of Determination

RE – Red Edge

RF – Random Forest

RGB – Red, Green and Blue

ROI – Region of Interest

RMSE – Root Mean Squared Error

RS – Remote Sensing

RT – Regression Tree

UAV – Unmanned Aerial Vehicle

VF – Vegetation Fraction

VI – Vegetation Index

VIF – Variance Inflation Factor

Abstract

Crop yield prediction and mapping are essential for crop management and decision-making. Advances in remote sensing (RS) and machine vision have significantly facilitated the development of non-destructive crop mapping in precision agriculture. In recent years, lightweight unmanned aerial vehicles (UAVs) have been widely used for the acquisition of high-resolution imagery for monitoring and evaluating crop growth and development. In this study, a cost-effective yield mapping workflow was designed and implemented in a commercial setting. Two UAVs were deployed to rapidly obtain RGB and multispectral images of many spinach fields in multiple stages of growth to assess spinach physiological attributes in the field environment. Based on the imagery, we proposed an image processing workflow for farm field orthoimage rotation and segmentation. Then, twelve vegetation indices (VIs) were extracted from the processed images, and the most robust VIs were selected by comparing the correlations among the VIs and yields, regression tree and stepwise multiple linear regressions. Excess Green Index (ExG) and Normalized Difference Vegetation Index (NDVI) were identified as two of the most robust VIs for predicting spinach yield at various stages of growth. A linear regression model was built with 45 calibrated plots and achieved a coefficient of determination (R^2) of 0.977. The optimal root mean squared error (RMSE) achieved on an external validation dataset was 0.192 kg/m with a mean absolute percentage error (MAPE) of 9.0%. The produced yield maps provided a basis for farm harvesting decision-making and crop management.

Résumé

La prévision et la cartographie du rendement des cultures sont essentielles pour la gestion des cultures et la prise de décision. Les progrès de la télédétection et de la vision artificielle ont considérablement facilité le développement de la cartographie non destructive des cultures dans le cadre de l'agriculture de précision. Ces dernières années, les drones légers ont été largement utilisés pour l'acquisition d'images à haute résolution afin de surveiller et d'évaluer la croissance et le développement des cultures. Dans cette étude, nous avons conçu et mis en œuvre un processus rentable de cartographie des rendements dans un contexte commercial. Deux drones ont été déployés pour obtenir rapidement des images RVB et multispectrales de nombreux champs d'épinards à différents stades de croissance afin d'évaluer les attributs physiologiques des épinards dans l'environnement du champ. Sur la base de l'imagerie, nous avons proposé un processus de traitement d'image pour la rotation et la segmentation de l'ortho-image des champs agricoles. Ensuite, douze indices de végétation (VI) ont été extraits des images traitées, et les VI les plus robustes ont été sélectionnés en comparant les corrélations entre les VI et les rendements, l'arbre de régression et les régressions linéaires multiples par étapes. L'Excess Green Index (ExG) et le Normalized Difference Vegetation Index (NDVI) ont été identifiés comme deux des VI les plus robustes pour prédire le rendement des épinards à différents stades de croissance. Un modèle de régression linéaire a été construit avec 45 parcelles calibrées et a atteint un coefficient de détermination (R^2) de 0,977. L'erreur quadratique moyenne optimale (RMSE) obtenue sur un ensemble de données de validation externe est de 0,192 kg/m avec un pourcentage d'erreur absolue moyenne (MAPE) de 9,0 %. Les cartes de rendement produites ont servi de base à la prise de décision en matière de récolte agricole et de gestion des cultures.

Acknowledgments

I am deeply indebted to my thesis supervisors, Dr. Shangpeng Sun and Dr. Viacheslav Adamchuk, for their guidance, support, and patience throughout the entire process of my master's degree study. Their expertise and encouragement were invaluable to me. I could not have completed this work without their help.

I would like to express my sincerest gratitude to Agriculture and Agri-Food Canada (AAFC) AgriRisk Initiative for their valuable support and funding, which enabled me to conduct research on the development of crop quality/quantity estimation methods using UAV imagery, ultimately leading to the successful completion of this thesis.

I would like to express my appreciation to Drone des Champ and Veg Pro International for involving me in this program. Their expertise in agriculture, crop management and remote sensing made the experiments go smoothly. I also appreciate their quick response throughout our collaboration.

I would like to thank Dr. Dingwen Tao, who guided and encouraged me during my undergraduate research. The experience and training I received from him motivated and encouraged me to face the challenges I encountered in my research.

I would like to sincerely thank my parents for their unwavering support and company. Their love and understanding helped me to focus during the challenging times. Their efforts and care allowed me to pursue my goals without hesitation.

I want to take a special moment to thank my partner, Yang Lu. I am truly grateful to have him as my partner who supports my academic pursuits.

Contribution of Authors

This thesis was authored by Xintong Jiang, with revision and critical review provided by Dr. Shangpeng Sun and Dr. Viacheslav Adamchuk for all the chapters.

Chapter 1 was authored by Xintong Jiang to describe the rationale and objectives of the study.

Chapter 2 was authored by Xintong Jiang. Xintong Jiang conducted comprehensive literature review related to the objectives in this thesis.

Chapter 3 was authored by Xintong Jiang, describing the methodology employed to carry out the study. The experiment and the data collection protocol were designed and conducted by Dr. Viacheslav Adamchuk and Dr. Shangpeng Sun and Xintong Jiang. UAV flights were operated by Gil Weisman from Drone Des Champs. The spinach fields and the external validation dataset were provided by Vert Nature Inc.

Chapter 4 was authored by Xintong Jiang, presenting the results and discussion of the study. The data processing, data analyses and discussion of the results was designed and conducted by Xintong Jiang, under the supervision of Dr. Shangpeng Sun and Dr. Viacheslav Adamchuk.

Chapter 5 was authored by Xintong Jiang, concluded the findings of the research.

Chapter 1. Introduction

1.1 Background

The world is facing food challenges due to the rapidly growing global food demand, environmental degradation, and extreme weather disasters [1-3]. Food security requires the sustainability of agricultural resources, tracking agriculture production processing and timely adjustments reflected in the policies related to food security [4]. Precision Agriculture (PA) provides solutions using a variety of techniques including sensors, machine vision, and spatial analysis to conduct effective assessments of crop conditions and to advise on site-specific crop management while maintaining environment quality. Notwithstanding the success of numerous PA applications since the mid-1980s, obstacles remain in adapting PA techniques for use in commercial agriculture [5]. In a commercial setting, it is preferred to have yield prediction as early as possible to arrange harvesting activities with limited resources including labor, protection and storage, and supply chain [6-8]. However, the uncertainties and variations in real-world farming pose a challenge to develop accurate and rapid yield prediction.

The traditional measurement of the physiological characteristics of plants is typically conducted manually in the field. Such measurement is time-consuming, labor-intensive, and destructive. The advancements in remote sensing (RS) have expanded the scope and capabilities of sensors, enabling retrieving plant phenotypes with exceptional spatial, spectral, and temporal resolution without destruction [9, 10]. With imagery obtained from RS, accurate and precise measurements and evaluation of crop traits can be obtained in a short time, significantly improving site-specific crop management. The quality and quantity of RS data collection are

influenced by the setup of the equipment and operations. Instead of counting on rough estimates or approximations, it is crucial to conduct extensive testing to develop a thorough protocol for data collection and processing.

Yield mapping is a crucial PA tool for crop management. Early prediction of yield can rank the priority of harvesting activities and guide subsequent production processes. Yield prediction models are primarily constructed using two categories of algorithms; these are machine-learning (ML)-based algorithms and linear regression [11]. ML-based algorithms are powerful tools to extract high-dimensional patterns but typically require a sustainable amount of data for training. Acquisition of many calibrated samples in commercial farm fields to create the training dataset is expensive and destructive. In contrast, statistical regression models can effectively describe the relationship between the observations and the dependent variables with limited data and computational resources. While previous studies with statistical regression models have achieved desirable results in yield prediction tasks, little has been written on yield prediction of leafy vegetables with extremely dense canopies.

1.2 Objectives

The main objective of this study is to investigate the feasibility of conducting fast and cost-effective yield mapping of spinach, which is a quintessential leafy vegetable with an extremely dense canopy. The proposed yield prediction can be conducted using a multiple linear regression model calibrated with a limited number of representative samples. In this study, we also aim to explore the representative power of the multispectral UAV imagery scanned from

different flight altitudes and to determine the optimal flight height that balances the information loss and scanning time.

This thesis is organized into five chapters, providing a systematic exploration of the research objectives. In Chapter 2, we reviewed the background and previous work of RS, yield mapping, and statistical considerations related to the development of the yield prediction model. In Chapter 3, we introduced the methodology of our experiments, including the protocol applied during data collection, the estimation of vegetation indices of the crop canopy traits and statistical analyses of the calibrated data. Chapter 4 is devoted to the discussion of the results and challenges encountered during the study with proposed solutions. We also discussed the potential future work which is an extension of our current study. Chapter 5 summarizes this study and provides a conclusion of our experiments and findings.

Chapter 2. Literature Review

2.1 Remote Sensing

The field of remote sensing (RS) has experienced significant advancements with the progression of sensor capabilities, data processing, and information infrastructure. Advanced RS techniques have been widely applied for the acquisition of high spatial and temporal solution imagery in many application areas. Compared to traditional data collection methods which are usually labor-intensive, RS provides a cost-effective and rapid solution to precision agriculture (PA) objectives and high-throughput plant phenotyping [12]. There are mainly three kinds of platforms used in remote sensing techniques: spaceborne, airborne, and ground-based [13]. Spaceborne includes satellites which provide large-scale spatial coverage but at relatively low resolution. For example, the spatial resolution of a Moderate Resolution Imaging Spectroradiometer (MODIS) image ranges from 250 m to 1000 m. The ground sample distance (GSD) of a Landsat satellite image is typically more than 10 m. In addition, the revisitation time of a typical satellite RS is 16 days on average, which is not compatible with the short life cycles of some crops [14]. Ground-based RS, although suitable for small-scale monitoring, is limited by its poor mobility [15]. The capability of Ground-based RS is also restrained by its long scanning time and small coverage. Airborne platforms, such as UAVs, provide non-destructive assessments with great flexibility [15]. The flexible revisitation period of UAVs and the low flight altitude of UAVs enable the acquisition of high spatial and temporal solution imagery. In addition, UAVs enable variable customization of flight setups at low operating costs.

In recent years, UAVs have come into prominence for the image acquisition of PA applications to assess the above-ground canopy traits of crops. The ground sample distance (GSD) of RGB UAV imagery is usually below 5 cm/pixel, providing ultra-high resolution imagery for PA applications such as crop growth monitoring, anomaly detection, and plant counting [16]. However, one of the limitations of UAVs is their relatively low power capacity, less than 2 hours per flight. In studies that require detailed images of crop canopies, the flight altitudes employed are usually around 20 m to 30 m [17-19]. However, low-altitude flights require a prolonged scanning time and multiple battery recharges that interrupt data acquisition. In the outdoor scenario, varied environmental conditions including changes in weather, illumination levels and shadows appear and introduce variations in the UAV imagery, resulting in decreased quality of the resulting UAV imagery [20]. Thus, employing a higher flight altitude while leveraging the information loss and scanning time is crucial to UAV imagery collection.

2.2 Vegetation Index

Existing studies promote vegetation indices as metrics to track the physiological dynamics of key traits of crops such as biomass, leaf area index (LAI), and nitrogen levels. Various optical VIs have been developed for qualitative and quantitative assessment of vegetative covers by obtaining electromagnetic wave reflectance information from canopies using passive sensors [14]. Typically, VIs are calculated by combining optical spectral bands in linear, or nonlinear operations. Their design aims to maximize sensitivity to vegetation characteristics while minimizing confounding factors such as soil background reflectance and atmospheric effects [21, 22]. Besides the RGB bands, other common multispectral bands include near infrared (NIR) and red edge (RE). For vegetation, the reflectance in both R and B bands are

low while high in the G band. The reflectance from the NIR band is significantly higher than the visible bands. However, the resolution of multispectral UAV images is generally lower than RGB images. For some models of multispectral sensors, a thermal band is also included to capture thermal infrared (TIR) images.

Normalized Difference Vegetation Index (NDVI) is one of the earliest proposed VIs and has been widely used in discriminating vegetation areas from bare soil and water [23, 24]. Previous studies determined NDVI to be the most stable VI for LAI estimation [25, 26]. For example, [27] demonstrated a strong positive correlation between the NDVI values derived from multispectral UAV imagery across the wheat growth cycle and grain yield. Their study examined the capability of NDVI to reflect the yield variation resulting from irrigation treatments and genotypes. However, many researchers have discussed the limitation of NDVI in terms of its low saturation threshold when applied to dense crop canopies [28, 29]. Thus, more sensitive multispectral VIs such as Green Normalized Difference Vegetation Index (GNDVI) and RE-based VIs such as Normalized Difference Red Edge (NDRE), and Chlorophyll Index - Red Edge (CI-RE) were used for yield prediction. For example, [30] evaluated the correlations between maize yield and 10 VIs and determined CI-RE and NDRE as the most promising VIs for maize yield prediction. [31] identified the G-B VI as the most robust VI for barley leaves across four growth stages. It demonstrated that specific VIs work effectively at certain growth stages of crops but are inadequate at other stages. When applied to different vegetation cultivars and environments to perform certain tasks, the specific VIs for evaluation and measurement should be tailored. In fact, the most robust VIs throughout the target life stages need to be determined.

2.3 Crop Yield Prediction and Mapping

Crop yield prediction is crucial to address global food issues. Effective yield prediction can assist crop management and decision-making. It is a complex question that must combine the effects from multitudinous factors to determine yield [32]. Many yield predictions focus on the effect of genotype, environment, and management [32-34]. In recent years, yield prediction with VIs and calibrated yield samples has become popular with the advancements that have been made in RS. Most studies collect multitemporal yield data across multiple growth stages and possibly even years.

Based on meta-analyses of crop yield prediction studies, machine-learning (ML)-based algorithms and linear regression are the two most frequently used approaches [11]. ML-based algorithms such as Neural networks (NN), Random Forest (RF), and Support Vector Machines (SVM) have proven their predictive power on crop yield and are leading the trend in recent decades [34-36]. Notwithstanding the capability of ML models on high-dimensional relationships and patterns, a sustainable amount of data is typically required to train ML models. Acquisition of this level of calibrated sample plots in commercial farm fields is expensive and destructive. In contrast, statistical regression models offer more cost-effective solutions to conduct yield prediction tasks. With a limited amount of data and computational resources, regression models explicitly examine the main effects and interactions between independent variables on the dependent variable. Previous studies with statistical regression models have achieved desirable results in yield prediction for red fescue, corn, soybean, and barley leaves [31, 32, 37].

Crop yield maps are important PA tools for site-specific crop management and crop monitoring [38]. The yield variation from systematic, image processing and random errors

reflected in yield maps can be applied to optimize the processing workflow of yield mapping and production. A general workflow of yield mapping includes preprocessing and interpolation of raw data, specific processing operations and statistical evaluation of the results [39].

2.4 Statistical Consideration

2.4.1. Multiple Linear Regression

Linear regression equations are usually approximations of the true relationship between several independent variables and one dependent variable. In multiple linear regression, the model has multiple regressors to describe the linear relationship between the regressors and the dependent variable. A general equation for a linear regression model is presented in (1). We consider the standard linear regression model:

$$y = X\beta + \epsilon, \tag{1}$$

where β is a $q \times 1$ vector for regression coefficients; X is an $n \times q$ matrix with the first column filled with ones; ϵ is an $x \times 1$ vector of unobserved random errors following $N(0, \sigma^2)$.

There are four assumptions of linear regression that should be examined before making inferences and predictions using the linear regression model [40, 41]. The assumptions are listed as follows:

1. Normality: The residuals of the model are normally distributed.
2. Homoscedasticity: The variance of the error term, $Var(\epsilon)$, remains the same among the independent variables.
3. No autocorrelation: The residuals are independent of each other.

4. Multicollinearity: No pair of variables are highly multicollinear with each other.

These assumptions can be verified using residual diagnostic plots after fitting a linear regression model. Transforming variables can be applied to correct assumption failures. For example, if the normality assumption is violated, a potential solution is to apply the Box-Cox transformation [42]. The Box-Cox transformation considers an optimal exponent λ selected based on the observations to transform the dependent variables into close to normally distributed.

2.4.2 Variable Selection

The criteria for variable selection include the significance criteria, information criteria, penalized likelihood, change-in-estimate criterion, and background knowledge [43]. Significance criteria are usually applied to decide the inclusion of independent variables. Hypothesis tests are the most popular significance criteria tool. The information criteria are mainly designed to measure model performance among a set of candidate models. For example, the Akaike information criterion (AIC) and the Bayesian information criterion (BIC) apply a penalization term on the model performance in proportion to the number of parameters included. Both AIC and BIC are maximum likelihood estimate-driven methods to evaluate the goodness-of-fit. For penalized likelihood, the least angle selection and shrinkage operator (LASSO), is used for high-dimensional model selection. Similarly, elastic net regularization and ridge regression are also not suitable to be applied to datasets of small sample sizes.

For correlation and multicollinearity among independent variables, correlation matrix plots provide explicit visualization of the degree of correlation. Variance inflation factor (VIF)

and condition index can be applied to determine the degree of multicollinearity to avoid the reduction in the significance of the independent variables.

Stepwise linear regression iteratively constructs a regression model by adding and removing independent variables and testing the significance by each iteration. However, stepwise linear regression has been criticized in multiple studies due to its proneness to overfitting, poor interpretability as well as biased and unreliable results [44, 45]. However, stepwise linear regression remains a popular tool for variable selection. Under some circumstances, a regression tree (RT) is considered an alternative to stepwise linear regression but more powerful in terms of combining interactions between independent variables. However, RT is also prone to overfitting and is not interpretable when the splits become very large.

2.4.3. Prediction Performance Evaluation

In this section, we discuss the evaluation of a fitted model from two aspects, goodness-of-fit, and predictive performance. While goodness-of-fit shows how the fitted model met the assumptions and performed on the same fitting dataset, the predive performance is used for internal and external validation [46, 47]. The most common performance measurement is the coefficient of determination (R^2) which measures the proportion of variation in the dependent variable that is explained by the regressors. However, R^2 is sensitive to the number of independent variables included in the model. The adjusted R^2 penalizes the number of regressors. Depending on the objectives and dataset, goodness-of-fit tests such the Pearson's Chi-Square test, G test and Kolmogorov-Smirnov tests can be applied.

Internal and external validation is used for verification of the predictive power of the fitted model. With limited data, internal validation based on resampling methods conducts model validation on the data from the same population fitting. Cross validation exemplifies the resampling process where the original dataset is randomly split into the training dataset and validation dataset. External validation, on the other hand, is conducted with another dataset, which might be different from the training dataset and thus, tests the robustness and generalization of the fitted model. It is suggested that a model with poor performance in internal validation is likely to fail in external validation [48, 49]. Thus, the order of validation is usually internal to external to avoid wasting resources on a poor model.

The metrics of model performance include root mean square error (RMSE), main absolute error (MAE) and mean absolute percentage error (MAPE). A survey on crop yield prediction identifies RMSE as the most used metric [11].

2.4.4. Influential Observations and Outliers

Influential points are defined as observations that change the slope of the line and have a significant influence on the fit of the model. These influential points can have a considerable impact on the regression solution and their inclusion needs to be considered carefully. Based on the diagnosis of regression, we consider three influential detection approaches, DFFITS, DFBETA and Cook's distance, which is based on deletion of one observation at a time [50].

DFFITS measures the changes in the predicted value for each observation, DFBETA measures the changes in the coefficients with one observation deleted at a time and Cook's

distance measures the overall changes in the fitted values. The formulas for the three measurements are as follows:

We consider the estimated regression model:

$$\hat{Y} = X\hat{\beta}, \tag{2}$$

where $\hat{\beta}$ denotes the estimated coefficient vector β, X denotes an $n \times p$ matrix of explanatory variables.

$$\text{DFFITS} = \frac{\left(\hat{y}_i - \hat{y}_{i(i)}\right)}{\sqrt{s(i)^2 h_{ii}}}, \tag{3}$$

$$\text{DFBETAS}_{ij} = \frac{\hat{\beta}_j - \hat{\beta}_{j(i)}}{\sqrt{MSE_i}(1 - h_{ii})}, \tag{4}$$

$$\text{Cook's Distance} = \frac{\sum_{j=1}^{n} \left(\hat{y}_j - \hat{y}_{j(i)}\right)^2}{p \times MSE}, \tag{5}$$

where $s(i)^2$ denotes the estimated error standard variance when the i^{th} row of X and y have been deleted, p denotes the number of regression parameters, h_{ii} denotes the i^{th}diagonal entry of the hat matrix, $H = X(X^T X)^{-1} X^T$, MSE denotes the mean squared error, p denotes the number of regression coefficients, $\hat{\beta}_j$ and $\hat{\beta}_{j(i)}$ denote the j^{th} estimated regression coefficient with and without the i^{th} observation being included in the regression model, respectively, and $\hat{y}_i$ and $\hat{y}_{i(i)}$ denotes the predicted value of i^{th} observation of with and without the i^{th} observation being included in the regression model, respectively.

Chapter 3. Materials and Methods

3.1 Data Collection

Field experiments were conducted in four spinach fields in 2021 and 2022 at VegPro International Inc., a commercial farm in Sherrington, Quebec, Canada. The overall data collection and processing procedure is described in Figure 1.

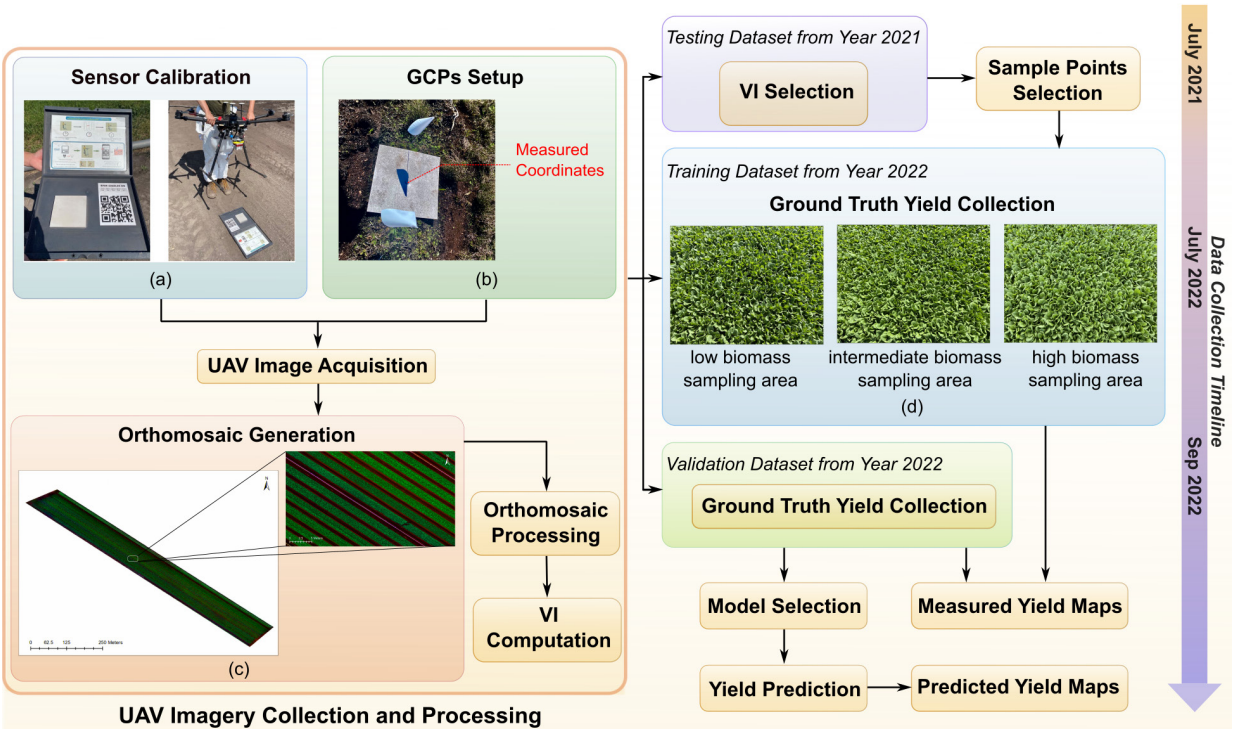

Figure 1. The data collection and processing protocol during the 2021 and 2022 growing seasons (a) The MicaSense ALTUM-PT multispectral sensor was calibrated with a MicaSense Calibrated Reflectance Panel (b) One of the GCPs placed in Field CA303. The white flags marked the GCP to prevent potential farm activity damage. (c) The RGB composite of the multispectral orthoimage obtained on July 15, 2022 (d) Three representative sampling areas with low, intermediate, and high biomasses that were manually harvested on July 22, 2022.

A DJI Phantom 4 Pro Drone with a 1-inch 20MP CMOS sensor (DJI Phantom 4 Pro Drone, SZ DJI Technology Co., Ltd., Shenzhen, China) was used to capture RGB photos, and a 12MP MicaSense Altum-PT sensor (MicaSense Altum-PT Sensor, MicaSense Inc., Seattle, USA) was attached to a DJI Matrice M600 Pro (DJI Matrice M600 Pro Drone, SZ DJI Technology Co., Ltd., Shenzhen, China) for multispectral image acquisition. The multispectral sensor has six bands (red, green, blue, near-infrared, red edge, and thermal) and was calibrated using a MicaSense Calibrated Reflectance Panel before the image collection. Figure 1(a) illustrates the calibration device and operation for the multispectral sensor before the flights. Six ground control points (GCPs) were placed across the field for georeferencing of the UAV images. Figure 1(b) illustrates an example of a GCP placed in the field. Two handheld global navigation satellite system (GNSS) receivers (Garmin eTrex 20x, Garmin Ltd., Olathe, USA) were used to record the geographic coordinates of the GCPs. The accuracy of the GNSS receivers was below 2 m.

Table 1 summarizes the information from the datasets collected over the two years. Throughout this period, a total of three rounds of image data collection were conducted, with one round in 2021 and two rounds in 2022. The spinach beds in all the tested fields were straight and parallel.

Table 1. Dataset Summary

Field	Seeding Date	UAV Imagery Collection Date	Harvesting Date
CA200	--	2021-Jul-15, 2021-Jul-19, 2021-Jul-21	--
CA303	2022-Jun-27	2022-Jul-15	2022-Jul-20 (Manual)
CA304	2022-Jul-04	2022-Jul-15	2022-Jul-22 (Manual)
CA221	2022-Aug-22	2022-Sep-12	2022-Sep-15 (Machine)

The first round of data collection in 2021 produced a testing dataset of RGB and multispectral imagery of a spinach field in its early, middle, and late stages. The time duration of each stage was less than one week. Figure 2 illustrates 6 orthomosaic maps constructed from the three stages. The testing dataset collected in 2021 employed a flight height of 70 m for the RGB sensor (ground sample distance (GSD) =1.92 cm/pixel) and 100 m for the multispectral sensor (GSD = 4.32 cm/pixel for the multispectral bands and GSD = 67.80 cm/pixel for the thermal band). As shown in Figure 2, both the RGB and multispectral images did not have sufficient details for canopy feature extraction, especially when describing canopy density levels. Additionally, the radii of sparse parts and unvegetated hollows observed in the spinach beds usually vary from 2 cm to 5 cm. Thus, the GSD should be equal to or smaller than the radii to accurately capture these unvegetated areas. Due to the higher resolution of the RGB sensor as compared to the multispectral sensor, a flight altitude of 70 m was also deemed impractical for the multispectral sensor. Thus, we adjusted the flight height to 50 m for both the RGB sensor (1.37 cm/pixel) and the multispectral sensor (2.16 cm/ pixel and 33.90 cm/ pixel) to balance UAV imagery collection time and canopy details in the imagery. With overlaps ranging from 75% to 80%, the average time used for scanning the two adjacent fields with 20 beds was approximately 0.5 hours.

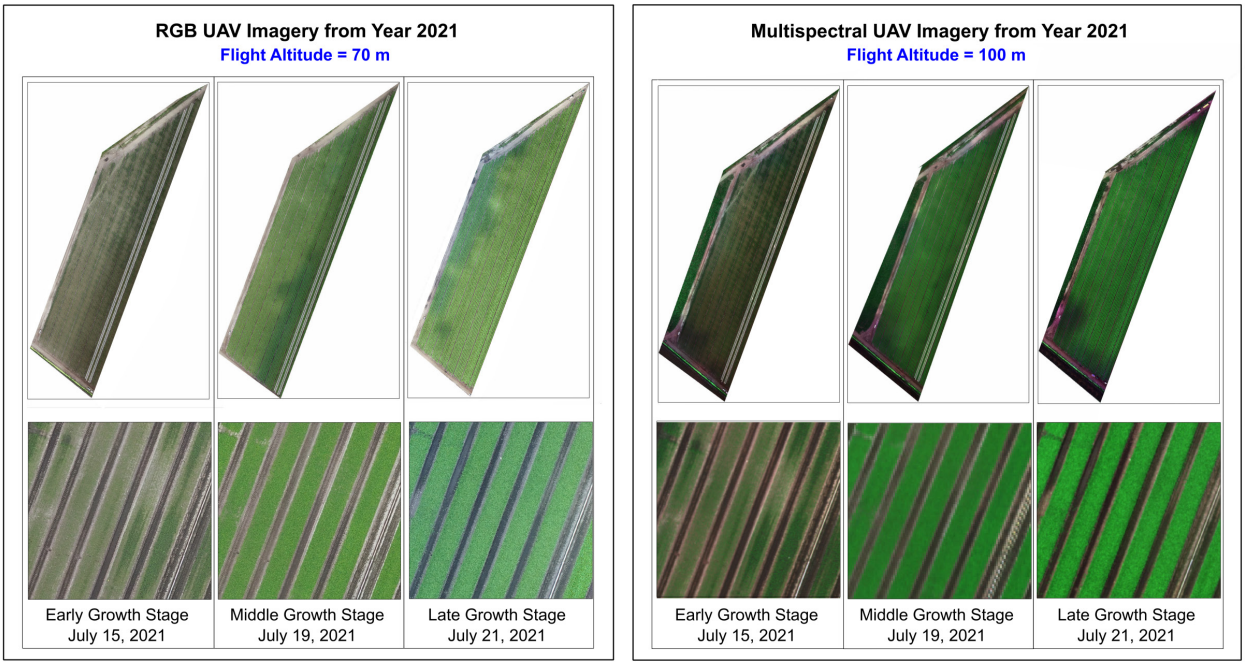

Figure 2. The first round of data collection in 2021 produced a testing dataset of RGB and multispectral imagery of a spinach field in its early, middle, and late stages of growth.

The second round of data conducted on July 15, 2022, contained RGB and multispectral imagery of two adjacent spinach fields, CA303 and CA304. This dataset was used as the training dataset for our multiple linear regression model. Figure 3 shows the crop growth conditions of CA303 and CA304 on the same day of the second round of UAV imagery collection. The spinach in CA303 had reached its late growth stage and was ready for net installation, which was used to protect spinach before harvesting. The spinach in CA304 was in its middle growth stage with small leaf sizes. While the canopy in CA303 was dense and covered most parts of the beds, the soil in CA304 was not fully covered by the spinach canopy. Based on testing results on the first dataset, two VIs, GNDVI and CI-RE, were used as references to process pre-arrival sample selections of CA303 and CA304, respectively. Details of the VIs calculation are introduced in Section 2.3. The 24 target beds covered in the UAV imagery were partitioned into unit cell sizes

with the width for each bed and length of 0.5 m. Additionally, we manually harvested 50 samples as the ground truth data to calibrate the yield prediction model. The harvested dataset consists of a similar number of samples with low, intermediate, and high biomass. Figure 1(d) illustrates three representative samples that were measured to have different levels of biomass on July 22, 2022. Before the manual harvest, the weeds within the sampling areas were removed, and the areas with observable anomalies were excluded from the collected dataset. The actual harvested locations of each preselected GNSS sampling area and the corresponding bed indices were recorded. The third dataset was collected in September 2022 for external validation for the developed prediction model. This dataset contains RGB and multispectral imagery of another spinach field, CA221, which was in its late growth stage. This dataset containing 30 sampling areas in CA221 was harvested by machine. To imitate the harvesting style of tractors, the farm beds were partitioned into unit cells with lengths of 0.5 m and widths matching the respective bed (approximately 1.6 m).

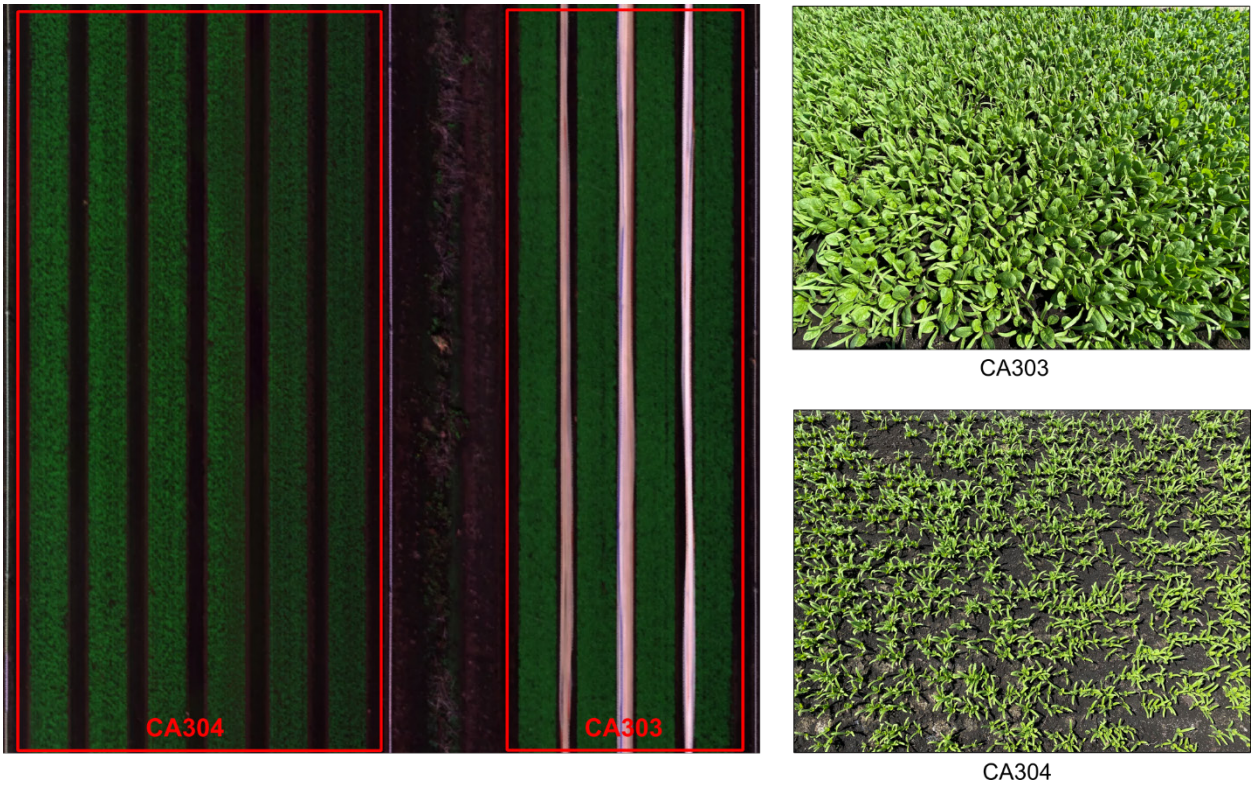

Figure 3. Fields CA303 and CA304 on the day of UAV imagery collection, July 15, 2022. Field CA303 was at the late growth stage while CA304 was at the middle growth stage.

3.2 Image Processing

After the image acquisition, photo stitching and orthomosaic generation were conducted using Agisoft Metashape (Agisoft Metashape 2.0 professional edition, Acuvec Geospatial, Calgary, Canada). The geographic locations of the six GCPs were used to georectify the orthoimages.

3.2.1 Orthomosaic Rotation

The rectangular shape of raised beds offers an advantage in partitioning vertical orthomosaic maps. Using bounding boxes to annotate the boundaries of each bed in the field, annotation maps can significantly improve image processing, computation, and analysis. Leveraging this shape advantage, we propose an orthomosaic map rotation algorithm. First, a rectangular box perpendicular to the image's horizontal boundary is identified as the region of interest (ROI) for the rotation algorithm, primarily consisting of beds and walkways. The position of this ROI remains immutable during rotation. Since rotating large orthomosaic images consumes substantial computational resources, we divide the rotation process into an initial coarse rotation followed by more precise rotations. In the coarse rotation, we set the rotation degree range from 1 to 180 degrees. Afterward, we refine the rotation degree by moving the decimal point one place at a time during each iteration. For instance, if 45 degrees is determined as the coarse degree for rotation, the following iterations will test from 44.1 to 45.9 degrees, with an increment of 0.1 degrees per iteration. Using this approach, the image will only undergo 200 rotations. Figure 4 illustrates the algorithm finding the optimal rotation degree for an image with a specific ROI. It iteratively refines the rotation degree and minimizes the mean column

differences within the ROI. The *getColumnDiff* function calculates the difference between the maximum and minimum ExG values within a buffer created around each column in the rotated image's ROI. The size of the buffer is set to be approximately the same as the bed in the ROI. The algorithm returns the rotation degree that yields the smallest mean column difference.

Figure 5 illustrates examples of ExG transition within a ROI with accurate and inaccurate rotation. As shown in the mean ExG intensity plot of Figure 5, the mean of differences between the maximum and minimum mean values of ExG within buffers will only be maximized with the optimal rotation degree. As an example, the correctly rotated image shown in the orange plot gives an average difference much higher than the inaccurately rotated image shown in blue plot.

Algorithm 1 Image Rotation Algorithm

Require: image I, ROI R, buffer size b, decimal places p
Ensure: rotation degree i

$i \leftarrow \underset{x=1,2,...,180}{\text{argmin}}\ \textsc{getColumnDiff}(x)$ ▷ Coarse degree for rotation
for $j \leftarrow \log(p),\ \log(p)-1,\ ...,\ 0$ **do**
    $N \leftarrow \{i - 9 \times 10^j,\ i - 8 \times 10^j, ...,\ i + 9 \times 10^j\}$
    $i \leftarrow \underset{x \in N}{\text{argmin}}\ \textsc{getColumnDiff}(x)$ ▷ Precise degree for rotation
end for
return i

function $\textsc{getColumnDiff}(x)$
    $df \leftarrow$ empty list
    $I_R \leftarrow$ rotate I by x degrees
    for each col c_R in R of I_R **do**
        $B \leftarrow I_R(c_R - b : c_R + b,\ :)$
        $v_{\max} \leftarrow$ maximum value of ExG in B
        $v_{\min} \leftarrow$ minimum value of ExG in B
        Append $(v_{\max} - v_{\min})$ to the end of list df
    end for
    $df_{\text{mean}} \leftarrow \text{mean}(df)$
    return df_{mean}
end function

Figure 4. The algorithm to conduct the orthomosaic map rotation. The algorithm first estimates a coarse degree of image rotation in a range of 1 to 180 degrees, then the precise rotation degree is decided with the same function.

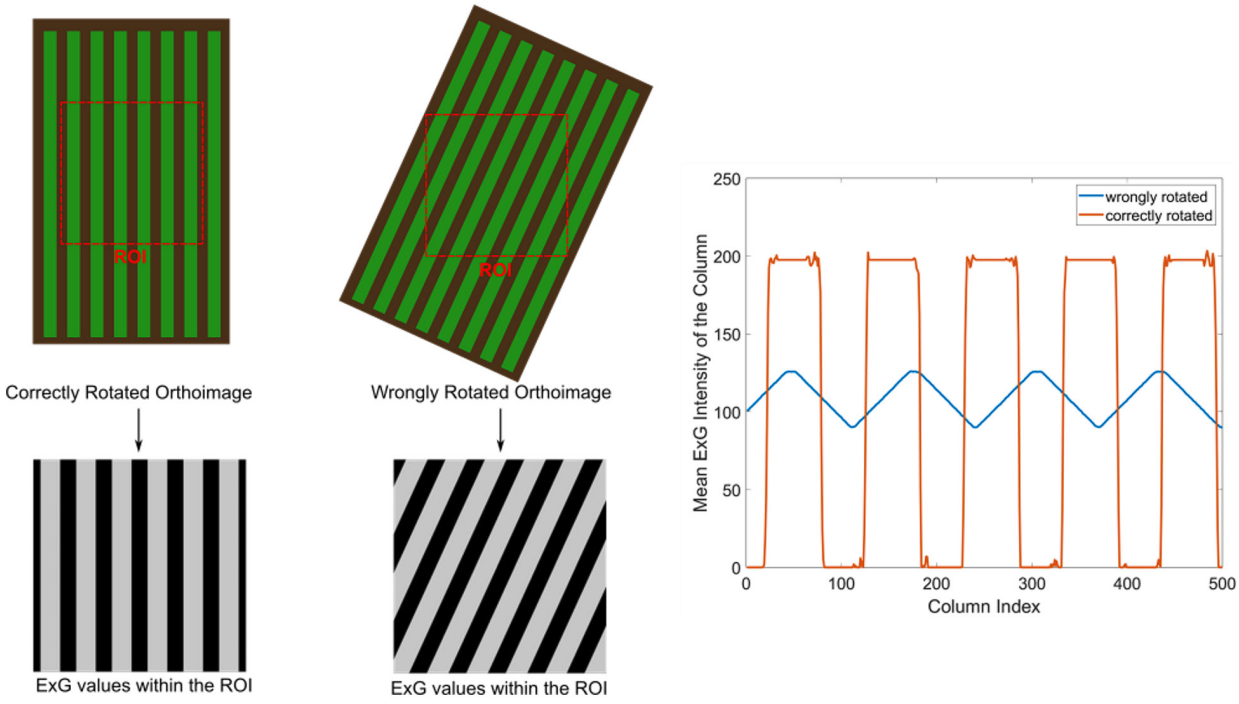

Figure 5. An example area selected as the ROI in the UAV orthomosaic of a spinach field in its early growth stage in July 2021 to determine the angle of rotation. A representative ROI of a relatively small size can significantly reduce the computation time of the rotation algorithm and reduce the portion of objectives unrelated to the rotation, such as the drive roads.

3.2.2 Bed Boundary Detection

Image thresholding and binarization were applied on the rotated images to distinguish raised beds and walkways between beds. The ExG-composite was used as the grayscale image for image binarization. A threshold was determined based on rough testing to classify the target orthomosaic image into the foreground with green canopy and the background that consists of soil and other objects. Following binarization, small objects with a limited number of connected components were eliminated since these are likely to be misclassified non-vegetated objects or weeds on the walkways. In this study, the threshold was determined by the 25th percentiles of the number of connected pixels of all objects included in the binarized image.

The subsequent bed boundary identification was carried out on the obtained binary image. In field environments, crops and weed often grow outside of delimited planting beds, which can complicate the identification of plant rows. To address this issue, we zeroed out all pixels present in a column with less than 80% vegetated pixels. This approach improved the accuracy of plant row identification by removing the noises. The delineation of vertical boundaries for each bed was conducted by iteratively looping through a selected range of rows to search for the transition points between zeros (background) and ones (foreground). The selected rows should all cross the same number of beds to obtain an equal number of transition points. If noise or small objects remain on the walkways of the binarized image, the row will be identified and skipped. The horizontal lines that contain the top and bottom nonzero pixels that fall within the vertical boundaries of each bed are marked as the corresponding horizontal boundaries. Figure 6 illustrates the corresponding pseudocode to identify the vertical boundaries of the beds. Since the lengths of beds within a field can be different and discrete, the ROI for boundary detection, R_B, should include all the targets beds. Otherwise, beds will be skipped during the iteration. If the same number of beds is encountered, the algorithm updates the boundaries accordingly. The algorithm skips rows with noise on the walkways and returns the final left and right boundaries of the beds.

Algorithm 2 Boundary Detection Algorithm

Require: Binary Mask B, a region selected including all beds of interest R_B
Ensure: The left and right vertical boundaries of beds LB and RB

$N_{\text{bed}} \leftarrow \infty$
for row i in R_B **do**
    $l_i \leftarrow$ positions of all transition points from zeros to ones
    $r_i \leftarrow$ positions of all transition points from ones to zeros
    $N_i \leftarrow \min(\text{length}(l_i),\ \text{length}(r_i))$ ▷ number of beds detected
    if $N_i < N_{\text{bed}}$ **then**
        $LB \leftarrow l_i$
        $RB \leftarrow r_i$
        $N_{\text{bed}} = N_i$
    else if $N_i == N_{\text{bed}}$ **then**
        $LB \leftarrow \min(l_i, LB)$
        $RB \leftarrow \min(r_i, RB)$
    else ▷ With noises on the walkways
        continue
    end if
end for
return LB, RB

Figure 6. The algorithm to conduct vertical boundary delineation.

In this study, beds were partitioned into uniform-sized cells with annotated boundaries. Offset buffers were created for each harvested sample to compensate for the inaccuracy in the GNSS coordinates measurements. Figure 7 illustrates an example of the buffered offset created for a harvested sample. Due to the GNSS bias, the actual sampling cell might be shifted from the preselected sampling area and the measured location. Thus, the two adjacent cells above and below the sampling area were used to construct the offset buffer. The statistical metrics of a sampling area, including mean, median, and VI computation, were obtained from all pixels within its corresponding buffer.

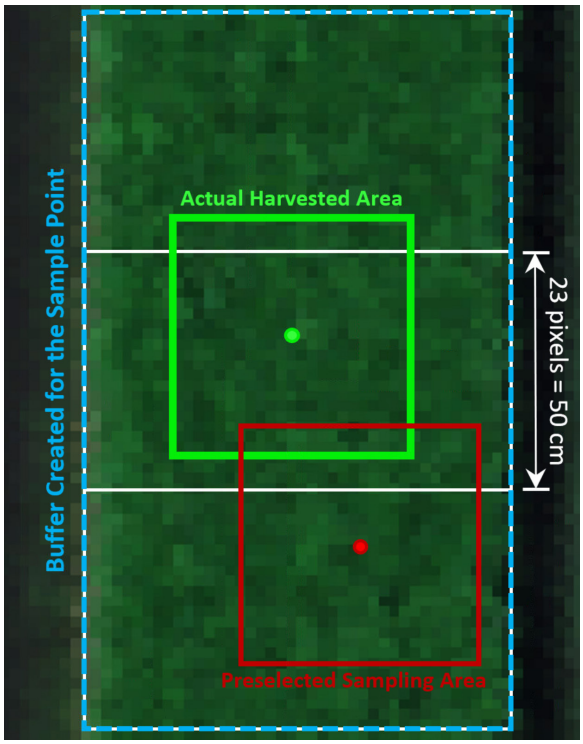

Figure 7. The buffer created for a manually harvested sampling area for the training dataset. The buffer (annotated by the blue bounding box) covered the three adjacent cells (annotated in white bounding boxes, respectively), which were created during the bed partitioning introduced in Section 3.1. The actual harvested area (annotated in the green bounding box) for this sample is shifted from its corresponding position selected before sample collection (annotated in the red bounding box) due to the bias of GNSS receiver.

3.3 Estimation of Vegetation Indices

A total of 12 multispectral-derived VIs that are related to crop yield and crop health conditions are selected as potential variables for the prediction model development. Table 2 lists the 12 selected VIs and the corresponding references. Non-zero values for VIs like ExG were observed in areas with zero biomass due to the color of the soil and other materials. We define an indicator named vegetation fraction (VF) to distinguish vegetated pixels from non-vegetated pixels. Specifically, we applied an NDVI threshold of 0.6 to differentiate the spinach pixels and

set the VI values of pixels below this threshold to zero. To decide this NDVI threshold, the approximate range of the threshold was first estimated via Otsu's method [51], followed by precise testing on the assessment ability of VF. As a result, VF was defined as the ratio of the number of pixels with NDVI > 0.6 to the total number of pixels within the target unit area.

Table 2. Potential VIs for spinach yield prediction

Vegetation Index	Computation Formula	Reference
Chlorophyll Index – Red Edge (CI-RE)	$\frac{NIR}{RE} - 1$	[52]
Chlorophyll Vegetation Index (CVI)	$\frac{NIR \cdot R}{G^2}$	[53]
Color Index of Vegetation (CIVE)	$0.441R - 0.881G + 0.385B + 18.78745$	[54]
Enhanced Vegetation Index (EVI)	$2.5 \times \frac{NIR - R}{NIR + 6 \times R - 7.5 \times B + 1}$	[28]
Excess Green Index (ExG)	$2G - R - B$	[55]
Green Leaf Index (GLI)	$\frac{2G - R - B}{2G + R + B}$	[56]
Green Normalized Difference Vegetation Index (GNDVI)	$\frac{NIR - G}{NIR + G}$	[57]
Modified Green Red Vegetation Index (MGRVI)	$\frac{G^2 - R^2}{G^2 + R^2}$	[58]
Nonlinear Vegetation Index (NLI)	$\frac{NIR^2 - R}{NIR^2 + R}$	[59]
Normalized Difference Red Edge Index (NDRE)	$\frac{NIR - RE}{NIR + RE}$	[24]
Normalized Difference Vegetation Index (NDVI)	$\frac{NIR - R}{NIR + R}$	[23]
Optimized Soil Adjusted Vegetation Index (OSAVI)	$(1 + 0.16) \times \frac{NIR - R}{NIR + R + 0.16}$	[60]

3.4 Choice of Variables and Sample Size

The total number of samples in the training dataset was 50, of which two samples were non-vegetated areas with zero biomass, and a sample deliberately collected from an area with observed anomalies. It was suggested that 10 samples for each variable in a linear regression model are the minimum requirement for accurate prediction and inference [45]. Thus, the number of variables in our multiple linear regression model was restricted to less than four. We first evaluated the empirical correlation matrix to find the VIs with the highest pairwise correlation among biomass, VF, canopy temperature and the 12 selected VIs, and avoided multicollinearity. Variance inflation factor (VIF) was also applied to assess the collinearity. Subsequently, RT and stepwise multiple linear regression methods were then utilized to rank the importance of VIs in accounting for the variation in biomass.

3.5 Model Selection and Validation

We consider a multiple linear regression model as follows:

$$Y_i = \sum_{i=1}^{k} \beta_i x_i + \epsilon_i, \tag{7}$$

where β_i are coefficients, x_i denotes the selected VI, ϵ_i denotes the error term and Y_i denotes the yield. In several cases, the model was fitted without intercept β_o since the yield will be zero when the VI and VF are both zero. After fitting, the assumptions of linear models were verified by the graphic assessment of residuals. The Box-Cox transformation will be applied to the dependent variable, i.e., the yield of the sampling area, if the normality assumption is violated. The best model was selected according to the adjusted coefficient of determination (R^2), Akaike

information criterion (AIC) and Bayesian information criterion (BIC). The optimal model should have the lowest values for AIC and BIC with the highest adjusted R^2, as this combination indicates better model fit and parsimony. After the optimal model was selected, influential observation diagnosis was conducted, which was important for our training dataset concerning its small sample size [50]. Specifically, we investigated potential outliers and influential observations that can distort the regression relationship and violate the assumptions using Cook's distance [61], DFFITS, and DFBETA [50].

The performance of the model was evaluated by the root-mean-square error (RMSE) and mean absolute percentage error (MAPE). A model with low RMSE and low MAPE on the validation dataset suggests good predictive power. The evaluation metrics were calculated as follows:

$$RMSE = \sqrt{\frac{\sum_{i=1}^{N}(y_i - \hat{y}_i)^2}{N}}, \tag{8}$$

$$MAPE = \frac{1}{N}\sum_{i=1}^{N}\left|\frac{y_i - \hat{y}_i}{y_i}\right|, \tag{9}$$

where y_i represents the measured ground truth yield of the target area, $\hat{y}_i$ denotes the predicted yield of the target area, and N represents the total number of sampling areas.

Bootstrapping validation and leave-one-out cross-validation (LOOCV) were conducted to evaluate the prediction power of the fitted model on datasets that are of a similar condition as the training dataset. We followed the internal-external validation procedure and first conducted internal validation for the proposed prediction models. Since poor performance in internal validation can foresee the failure of external validation [48, 49], models with inadequate results

in the internal validation phase would not be moved on to the external validation phase. For models with promising internal validation results, external validation was conducted with the third dataset from September 2022 to evaluate the generalizability of the proposed models.

Chapter 4. Results and Discussion

4.1 Image Processing

Figure 8 illustrates the representative results of each step for the orthoimage processing workflow. The original orthoimage in Figure 8(a) was stitched by the Agisoft software. As the first step, it was rotated to make all the beds strictly vertical, as shown in Figure 8(b). Figure 8(c) shows the resulted image from an optional subsequent step following rotation to add padding to the rotated image to eliminate blank spaces generated by the rotation operations. Then, we tested and chose an ExG threshold to binarize the rotated orthoimage. As Figure 8(d) shows, small objects such as weeds on the walkways were included in the mask. Thus, the next step removed objects with less than 100000 pixels in the mask, which was determined by the 25th percentage of the number of pixels for all connected objects. After this step, we still observed unclear boundaries with the presence of noises on the walkways and unremoved incompletely scanned bed in Figure 8(e). We then zeroed out all the columns with less than 80% valid pixels and obtained the results in Figure 8(f). The cleared mask was applied on the rotated orthoimage as the resulted image shown in Figure 8(g).

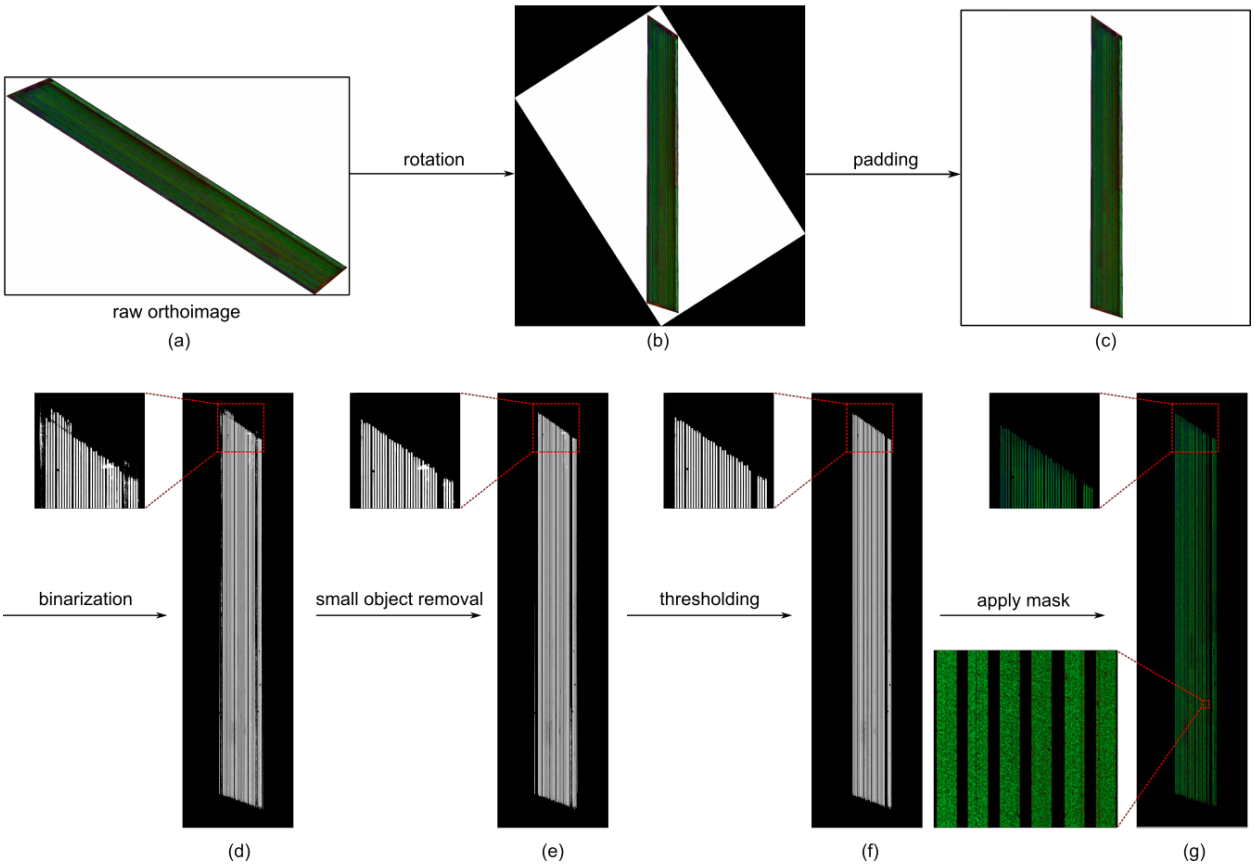

Figure 8. Representative results derived using the proposed image processing workflow

4.2 Correlations and Model Fitting

The correlation matrices of the VIs calculated from the 50 harvested samples in CA303 and CA304 are illustrated in Figure 9. Certain VIs were observed to significantly outperform other VIs during specific growth stages, such as the strong correlation between CI-RE, NDRE and late-stage biomass shown in Figure 9(a). However, Figure 9(b) shows that CI-RE and NDRE were weakly correlated with biomass during the mid-stage. Therefore, these two VIs were not robust enough to be applied for evaluating the relationship between biomass and canopy traits from mixed growth stages.

The results of all the tests conducted, including the correlation matrices in Figure 9, RT and stepwise multiple linear regression, consistently suggested that ExG was the most robust VI in determining the variation in spinach yield from the mixed growth stages. VF and MGRVI were ranked as the second and third most important variables. After comparing several combinations of variables and their interaction terms, the following multiple linear regression model was built.

$$Yield = 11.5859 \times ExG - 3.4680 \times (ExG{:}VF), \quad (10)$$

where $Yield$ denotes the yield harvested from a sampling area, ExG denotes the median value of ExG of vegetated pixels in this sampling area, VF denotes the vegetation fraction of the sampling area, and $ExG{:}VF$ denotes the interaction term between VF and ExG. There was no evidence of collinearity between ExG and VF in this model based on the VIF assessment. According to the adjusted R^2, AIC, and BIC in Table 3 and the ANOVA table comparison of the models in Table 4, the model M1, which provided the lowest AIC and BIC as well as a relatively high adjusted R^2 was determined as the best models in terms of parsimony and fitting results. With M1 selected as the optimal model, we conducted the influential points diagnosis with the training dataset. Five data samples were identified as influential points using Cook's Distance, DFBETA, and DFFITS. The size of the resulting training dataset without the influential points was 45. The fitted model satisfied the assumptions of the linear regression model and gave an adjusted R^2 of 0.977.

Table 3. Comparison of candidate models

Index	Model	Adjusted	AIC	BIC
M1	$Yield = ExG + ExG{:}VF$	0.9647	593.72	599.33
M2	$Yield = ExG + VF + ExG{:}VF$	0.9643	595.29	602.77
M3	$Yield = ExG + MGRVI + ExG{:}VF + MGRVI{:}ExG + MGRVI{:}VF$	0.9657	595.19	606.42
M4	$Yield = ExG + VF + MGRVI + ExG{:}VF + MGRVI{:}ExG + MGRVI{:}VF$	0.9649	597.09	610.18
M5	$Yield^{\lambda_1} = ExG + ExG{:}VF,$ λ_1 was derived from the Box-Cox Power Transformation	0.8736	~~1587.53~~*	~~1593.14~~*
M6	$Yield^{\lambda_2} = ExG + VF + ExG{:}VF,$ λ_2 was derived from the Box-Cox Power Transformation	0.8565	~~1552.39~~*	~~1559.88~~*

* Due to the different scales of the Box-Cox transformed model, the AIC and BIC values of M5 and M6 should not be compared with other untransformed models. However, we rejected the transformation in M5 and M6 since the linear assumption was not significantly improved by applying the Box-Cox transformation.

Table 4. Comparison of the ANOVA tables for the candidate models

Index	Residual Degrees of Freedom	Residual Sum of Squares	Degrees of Freedom	Sum of Squares	F-statistic	Pr(>F)
M1	46	583883				
M2	45	578640	1	5243	0.4154	0.5228
M3	43	531311	2	47330	1.8748	0.1660
M4	42	530159	3	1151	0.0912	0.7642

Similarly, M5 and M6 were not included in this comparison due to the scale difference.

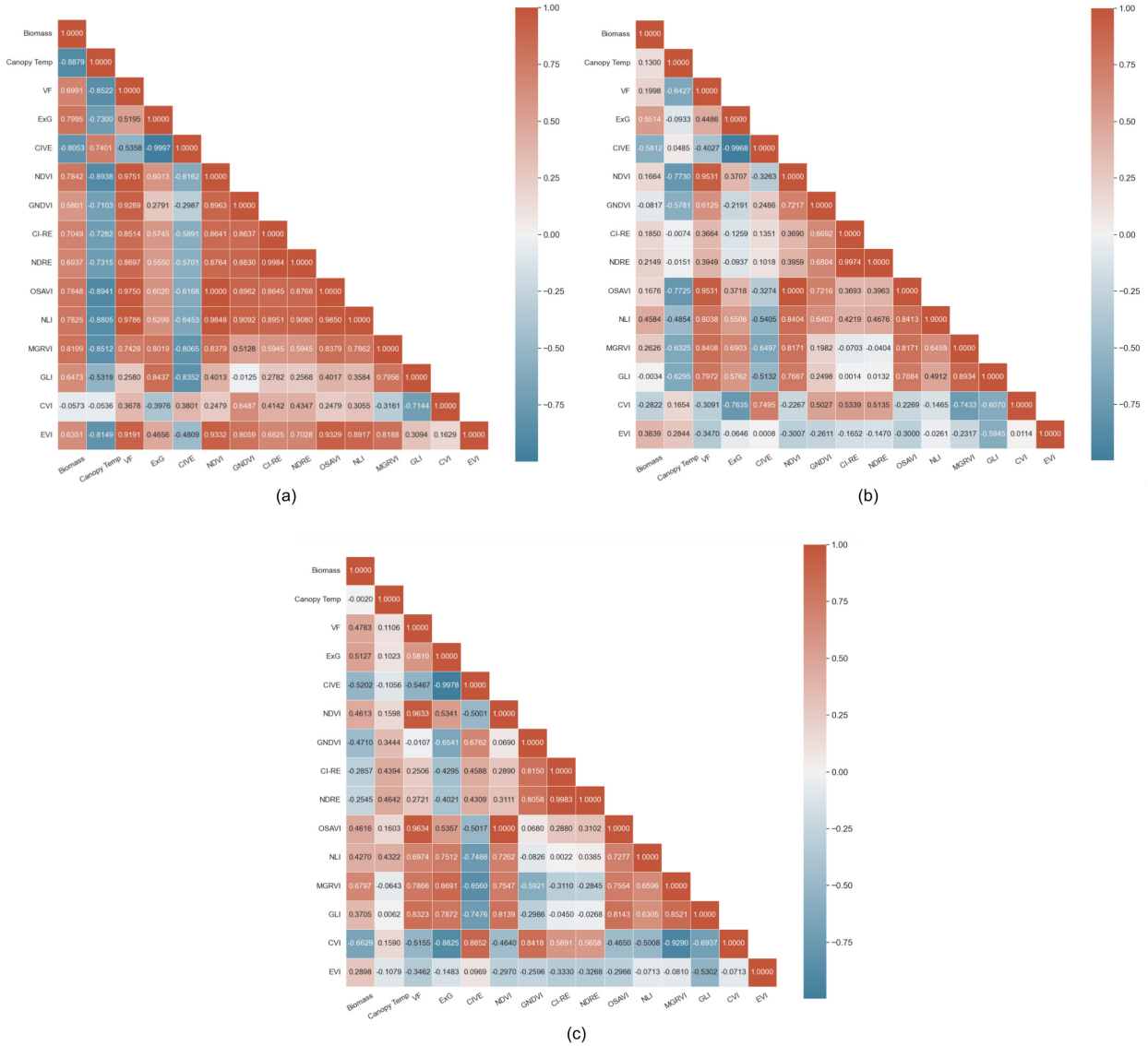

Figure 9. The correlation matrices between manually harvested biomass, canopy temperature and the 12 selected VIs of the training dataset. The magnitude of correlations is indicated by the color intensity of the cell. Red cells represent strong positive correlations while blue cells suggest negative correlations (a) Correlation matrix of the 15 data points from CA303, in which UAV imagery was collected 5 days before harvesting. (b) Correlation matrix of the 30 data points from CA304, in which UAV imagery was collected 7 days before harvesting (c) Correlation matrix of all the 50 data points from both CA303 and CA304.

4.3 Assumption Validation

We used the graphical assessment of the residuals to examine the assumptions. Figures 10 and 11 illustrate the graphical assessment obtained from R. Figures 10(a) and 11(a) show the residuals against the fitted values. The inward-opening funnel pattern in Figure 10(a) indicates that the $Var(\epsilon)$ increases as Y decreases. We observed the mitigation of the pattern in Figure 11(b) when the model is fitted without potential outliers. Figures 10(b) and 11(b) are the normal probability plot that examines the normality assumption. Both the left and right tails fall off the diagonal lines in Figure 10(b), while this violation is solved in Figure 11(b) with the influential observations excluded from the model fitting. The scale-location plots shown in Figures 10(c) and 11(c) also check the homoscedasticity assumption of the fitted models. Again, the pattern observed in Figure 10(c) becomes less obvious in Figure 11(c). Overall, we conclude the assumptions are better satisfied without the 5 identified influential points.

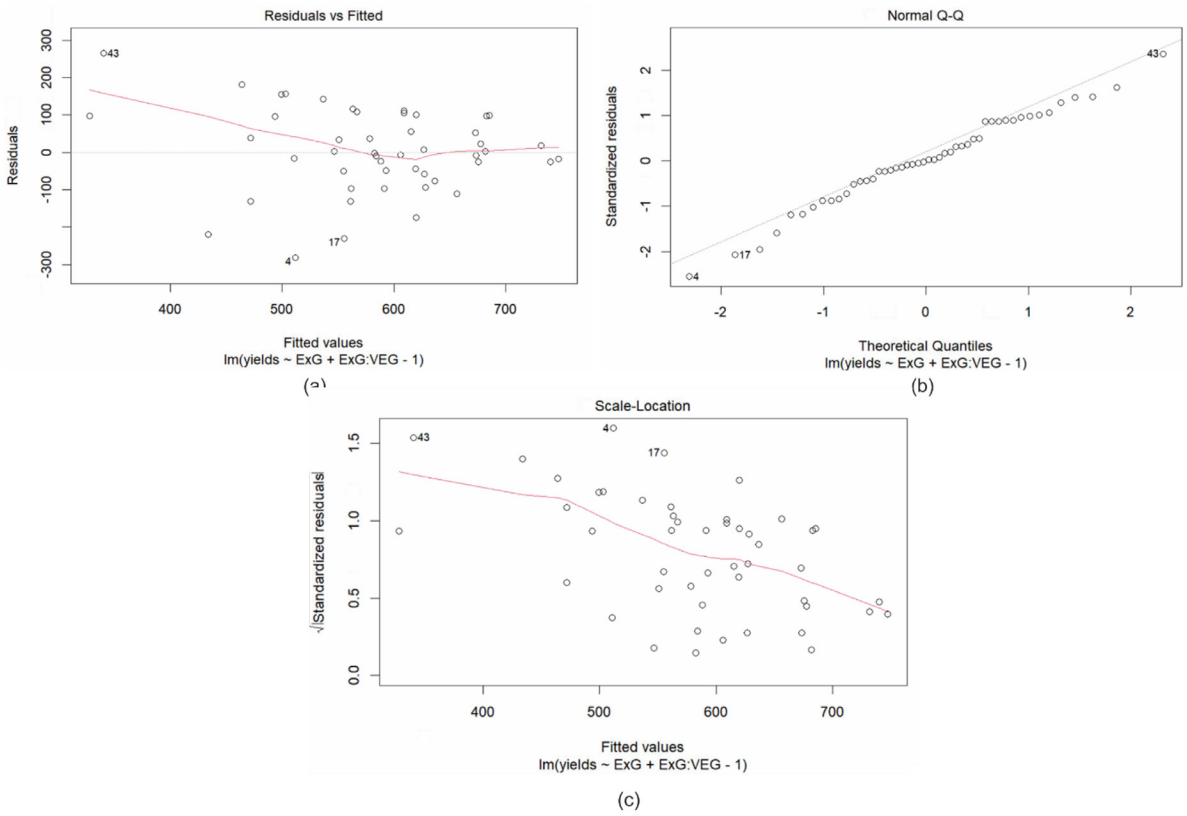

Figure 10. Assumptions verification of the model fitted with all observations.

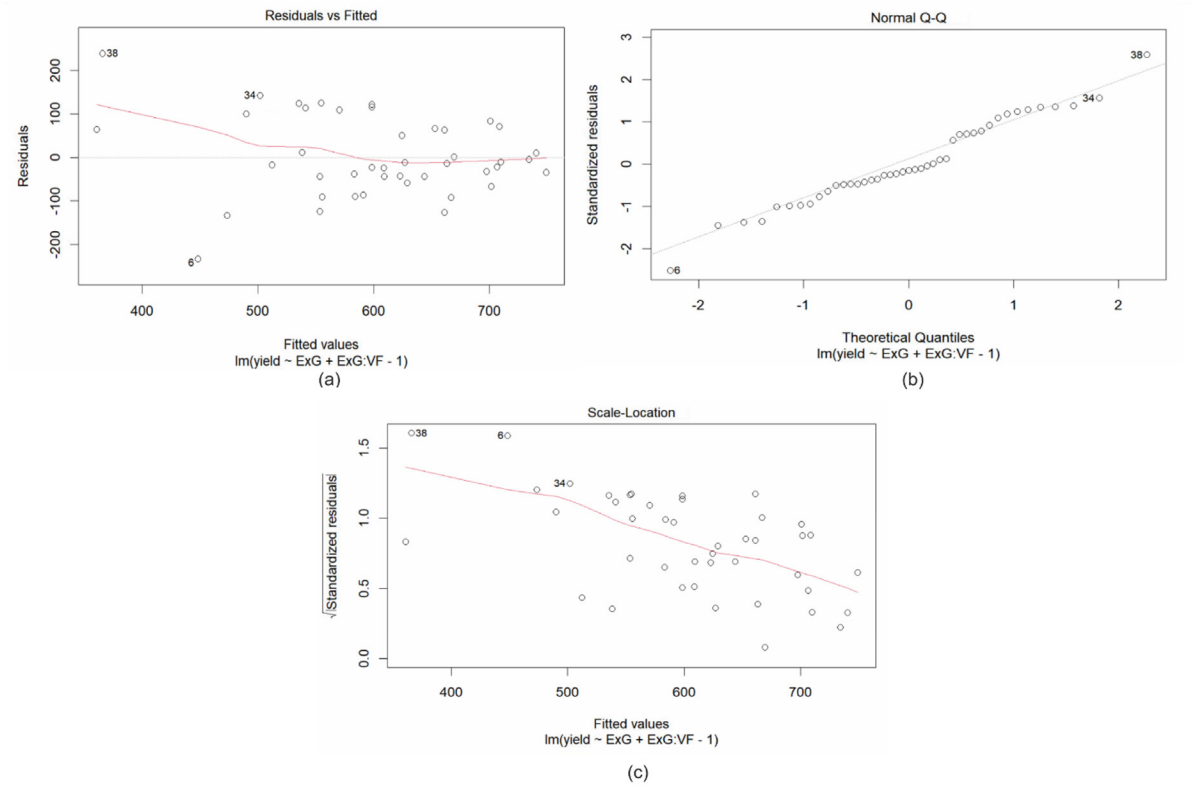

Figure 11. Assumptions verification of the model fitted without the 5 identified influential observations.

4.4 Model Validation

In our study, internal validation was first conducted using bootstrapping methods and Leave-One-Out Cross-Validation (LOOCV). An adjusted R^2 of 0.977 (95% confidence interval: [0.973, 0.987]) was obtained from 1000 bootstrap datasets, suggesting the stability of the model. A LOOCV conducted results in an R^2 of 1, with the RMSE equal to 0.305 kg/m.

Encouraged by the good performance in the internal validation, we conducted external validation with the dataset collected in September 2022 to examine the predictive power and robustness of the model. The validation dataset, however, was obtained from a later-stage spinach field compared to CA303 and CA304. In addition, the field was harvested by machine. Figure 12 illustrated two areas that were harvested manually and by machine. We noticed a heterogeneity introduced by different harvesting methods. Thus, a scaling factor of 1.198 was applied to the predicted results to account for this difference. The scaling factor was calculated by fitting a linear regression model with zero intercepting using prediction results versus the measured yield. Figure 13 and Table 5 illustrate the validation results. An MAPE of 20.9% was obtained over full validation samples. A subset of samples with medium-level of yields provided an RMSE of 0.192 kg/m with a MAPE of 9.0%, while the low-yield sample subset and high-yield sample subset only achieved an RMSE of 0.544 kg/m and 0.501 kg/m with MAPE of 39.2% and 19.4%, respectively.

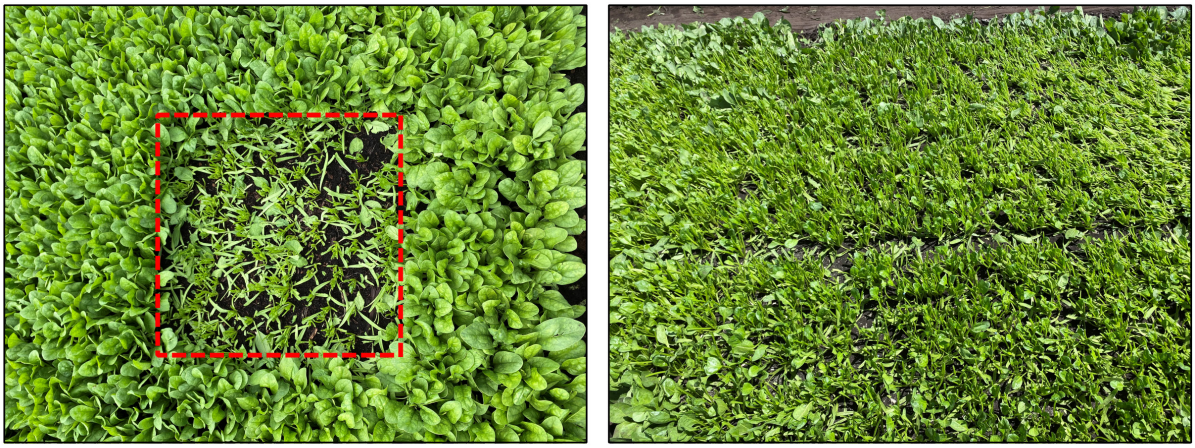

Figure 12. Comparing the leftovers from manual-harvested and machine-harvested spinach bed (a) A sampling area manually harvested in CA304 (b) A section of machine-harvested spinach bed

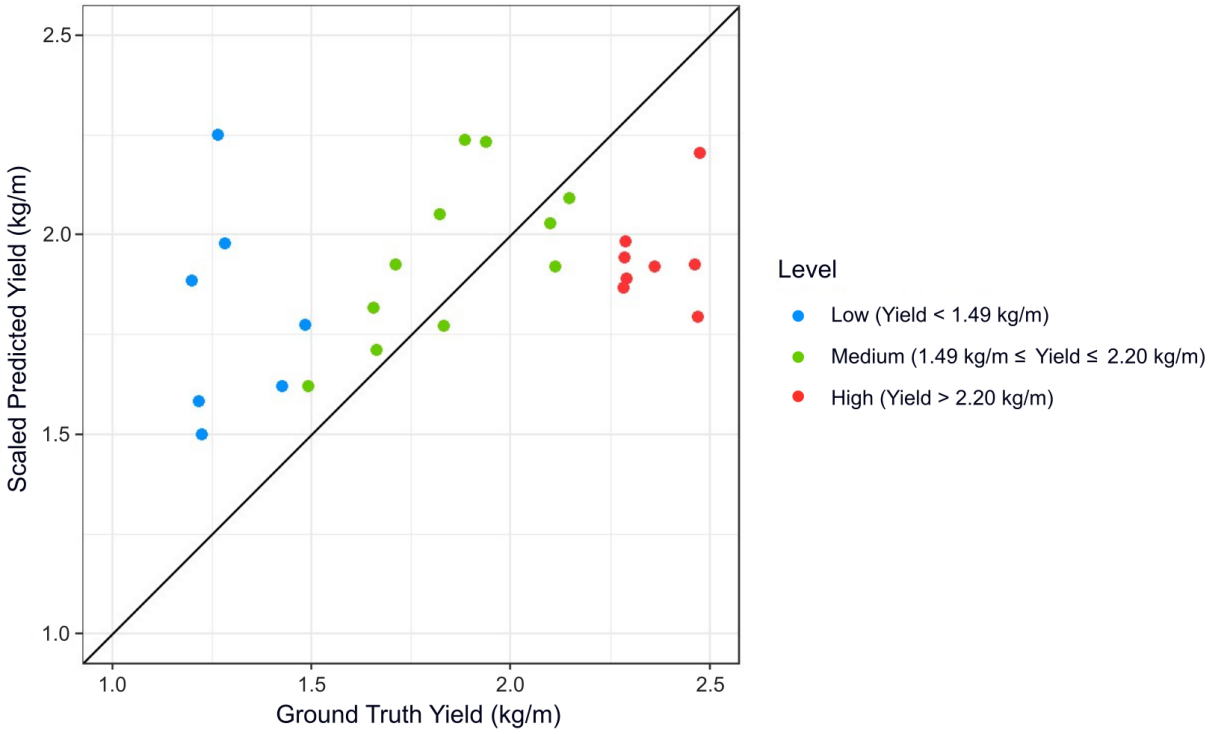

Figure 13. The ground truth yields versus the scaled predicted yield. The model gave a relatively low MAPE and RMSE for medium-level yields.

Table 5. External validation results from the September 2022 dataset

Ground Truth Yield Range	RMSE	MAPE
all validation data points	0.427 kg/m	20.9%
Yield < 1.49kg/m	0.544 kg/m	39.2%
1.49 kg/m ≤ Yield ≤ 2.20kg/m	0.192 kg/m	9.0%
Yield > 2.20kg/m	0.501 kg/m	19.4%

Figure 14 demonstrates the difference in the x-space between the training and external validation datasets. In the external validation dataset, most of the samples had higher ExG and VF values than samples in the training dataset. This difference between the training and validation datasets undermined an extrapolation issue in the model when applying it to unobserved data.

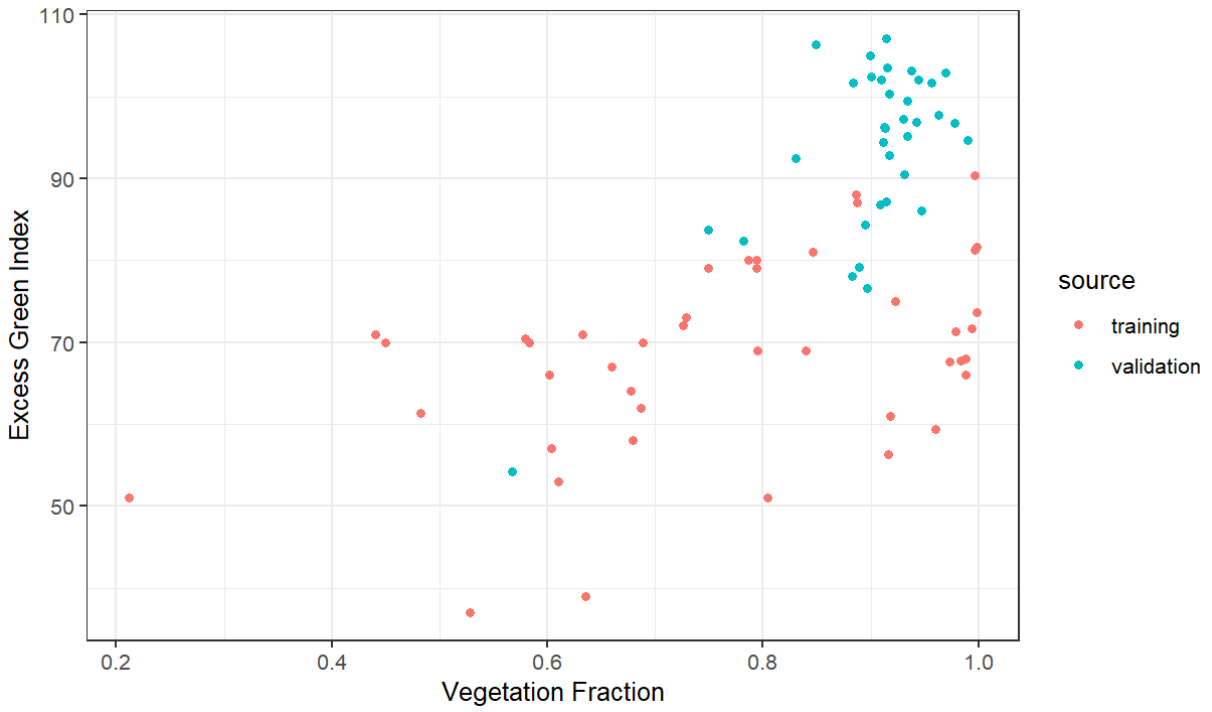

Figure 14. VF and ExG of the training dataset and the validation dataset. The validation dataset was from a later growth stage than both fields in the training dataset, which resulted in higher ExG and VF values.

4.5 Yield Mapping

Yield maps were generated as references for potential areas of interest. These maps offered overall visualization of field conditions and provided guidance for harvest priority ranking and site-specific crop management. In our experiments, the farm beds were partitioned into cell areas with a length of 0.5 m or 1 m depending on the areas to be covered in a single cell for machine harvest consideration. Such partition style imitated the harvesting style of machines. Figure 15 illustrates a map of the predicted yields of the CA303 and CA304 with a cell length of 1 m. The green colored cells in the map suggested high yields that should be assigned high priority during harvest. The red and yellow cells indicate low yields in these areas and potential anomalies such as water stress and disease. The map generated a spatial yield distribution that is

consistent with ground observations during the study and is suitable for use during the decision-making process.

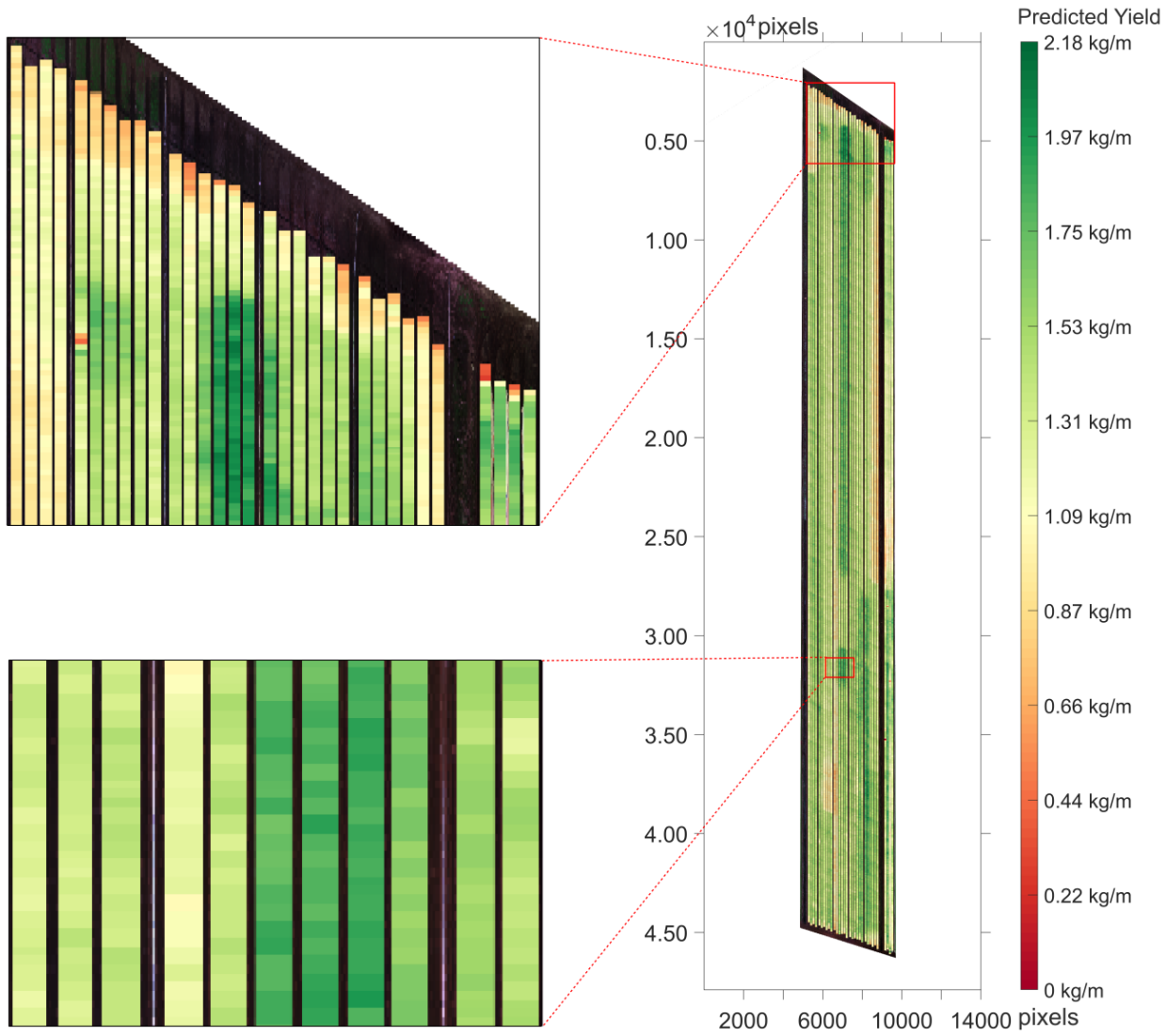

Figure 15. Predicted yield map for unit areas in fields CA303 and CA304 (unit area length = 1 m)

4.6 Discussion

In this study, UAV imagery was shown to be an effective tool to provide a quality representation of the spatial distribution of vegetation quantity and quality across the fields. While recent PA techniques are becoming more feasible in commercial agriculture settings, the adoption of PA techniques in commercial agriculture still faces barriers, such as the willingness of farmers to apply PA techniques [5]. In our study, we encountered multiple limitations in terms of the use of UAV imagery in an intensive crop production setting, including the conflicts encountered during the data collection steps. For example, due to essential protection operations from the weather and farm activities, spinach is normally covered with a net for the second half of vegetation and the net is removed shortly before harvesting. Thus, the UAV imagery collection took place at least 3 to 5 days before the netting and was used to predict the harvested crop. The time gap between the UAV imagery scanning and actual harvest time introduced unobserved variance, unquantifiable uncertainty, and confounders. Although relatively low vegetation coverage provided moderately uncertain predictions, most of the validation results indicated an ability to predict crop biomass to be harvested under 40%. Certainly, later imagery data will further reduce the uncertainty.

We proposed an image processing workflow for effective multispectral UAV imagery given the organized rectangular structure of the spinach beds in our study. This workflow is not suitable in studies for very sparsely distributed plants without clear plant rows or individual-level crop identification with low flight altitudes, as it relies heavily on the presence of well-defined rows and structured plant arrangements. Alternatively, NN can be employed to conduct semantic segmentation in this scenario [62]. In our dataset, we did not apply any image enhancement techniques due to the high color contrast between spinach and soil in the field. In cases where

vegetation pixels exhibit small differences from the background pixels, for example, images of crops in their early stages, image enhancement algorithms can be applied as additional image preprocessing steps to improve the visibility of plant features and structures. Candidate algorithms to increase the color contrast include the Retinex-based algorithm [63, 64], histogram equalization [65] and gamma correction [66].

In addition to the timing of image acquisition, contemporary harvest processes provided a limited number of harvested crop weight measurements with uncertainties in the location of the start and end of each cut. Only 50 samples of 50 × 50 cm were manually harvested for calibration to avoid severe destruction on the fields that would result in financial loss to the farm. We have also noted that cutting height was operator-defined and varied according to the crop conditions. As discussed in Section 4.4, image data calibration using manual harvesting may not be representative of machine harvesting. At the same time, machine harvesting did not always provide harvested biomass weight per well-defined area.

Overall, our prediction model fitted well on the training set and produced accurate prediction results on internal validation and the medium-level yield external validation samples. For the low-yield and high-yield samples in the external validation set, the model failed to produce close prediction potentially due to unmatched x-space. Restricted by the production plans and activities of the farm, the samples collected for external validation were at a later growth stage than the training set sample. Potential factors relating to the heterogeneity in yield, such as water stress, fertilization intensity, and diseases, might be unmeasured. These confounders related to environment, genotype and their interactions can be estimated from further measurement and evaluation [67, 68]. The empirical relationships derived from the data-driven models greatly depend on the calibrated experimental observations. The predictive power

of the model is constrained by the thoroughness of the training dataset and is at risk of extrapolation when applied to prediction. In our experiment, two handheld GNSS receivers were used to obtain the geographical locations of the samples. While cost-effective, the 2-meter bias of these receivers introduces errors in georeferencing. Buffer zones for each sample were employed to mitigate such errors. An alternative approach is to apply a real-time kinematic positioning (RTK) system to obtain more accurate and precise measurements with a bias of less than 3 cm [69].

Another source of errors came from the sensitivity of VIs when applying them on such extremely dense spinach canopies (i.e., high biomass area). For example, the effectiveness of NDVI in describing the vigor of spinach saturates as soon as it came to the middle to late stages of spinach growth. On the contrary, RE-derived VIs such as CIRE and NDRE that measure the chlorophyll content in the canopy are applicable for the mid-to-late stages of crops but have weak performance in the early stages [70, 71]. Thus, the saturation thresholds of VIs require further identification to establish their practical effective ranges of yield prediction of different crops, especially when mixed growth stages are involved in a dataset. Besides common VIs that have been proposed for general assessment, plant-specific and even cultivar-specific VIs can be defined using data mining and band fusion algorithms. [72] proposed a generalized vegetation index which has learnable weights for R, G, B and NIR bands. However, a substantial amount of data is required to train a convolutional neural network to construct the generalized VI.

During our data collection, we observed that the outdoor conditions in fields, including changes in the weather, illumination conditions, and cloud shade, had a significant influence on the quality of data collected. In many PA tasks, the dataset usually contains data from multiple growth stages and thus consists of multiple UAV images collected from different time slices.

Although we can mitigate the variance among images collected during a single flight of data collection via output normalization, the variance between data collected on different dates is more complicated. To address this issue, future studies might consider collecting data in a longitudinal format and analyzing the dataset by a linear mixed effect model. By adopting this approach, we increase the accuracy of prediction by accounting for the potential confounding factors during data collection and estimation of the variability between different flights, which will enable more accurate predictions.

In this work, we investigated the effectiveness of multispectral UAVs applied to assess high-level spinach canopy characteristics and subsequently applied these traits for VI estimations and yield prediction. During our testing, we tried to reconstruct the field surface with our UAV images. However, the small sizes and the dense canopy of spinach restricted us from achieving a precise 3D representation of the field. A potential aspect of future work would be to obtain more detailed crop physiological attributes such as plant heights and leaf sizes. This may be achieved by applying photogrammetry techniques and LiDARs mounted on tractors [73]. However, such ground-based RS is usually much more time-consuming and expensive compared to UAV imaging collection, which requires consideration of trade-offs between the coverage area, plant phenotyping quality and resource consumption.

In our study, we also see a significant imbalance between the number of UAV images and calibrated yield data. For example, we obtained more than 12000 unit-sized cells from a single UAV flight that completed 0.5 hours while having only 50 of these cells calibrated via manual harvesting in 2 hours. A prospective strategy to utilize the uncalibrated UAV images is to qualitatively assess the condition of the canopies via unsupervised learning techniques or semi-supervised learning [74]. Unsupervised learning techniques, such as clustering, can be utilized to

group similar UAV images together and detect patterns or anomalies. Although lack of accurate quantification of the objectives, these techniques can assist in pinpointing areas within the field that may need additional attention and prioritize high-yield areas [75, 76].

Chapter 5. Summary and Conclusions

In this study, we assessed the potential of conducting spinach yield predictions with VIs derived from multispectral UAV imagery acquired from a flight height of 50 m. This study first introduced a UAV orthomosaic image processing workflow which can significantly improve the efficiency of subsequent tasks. Based on a dataset collected from two adjacent spinach fields in their middle and late growth stages, ExG and NDVI-derived VF extracted from the multispectral UAV images were determined to be the most robust VIs for multiple growth stages of spinach. Compared to some previous studies, the relatively high flight altitude utilized in this study greatly shortened the UAV imagery collection time to reduce the possible variance and uncertainty induced by outdoor condition while leveraging the information loss due to the lower resolution. This study then developed a multiple linear regression model for spinach yield prediction using the estimated VIs. Despite using a small dataset with only 50 calibrated samples, the model fitted well on the training dataset and produced accurate prediction results on the medium-level yield validation samples, which achieved an RMSE of 0.192 kg/m and an MAPE of 9.0%. Currently, the predictive power of the model is restricted by the representative and accuracy of the calibrated samples. A potential strategy for further improvement is to minimize errors and uncertainty induced by the calibrated sample points while increasing the x-space coverage for the dataset. This can be achieved by collecting data from more growth stages. The challenge also lies in quantifying the confounding factors and unknown variables that occur between the collection of UAV imagery and harvest activities.

References

[1] C. Lesk, P. Rowhani, and N. Ramankutty, "Influence of extreme weather disasters on global crop production," *Nature,* vol. 529, no. 7584, pp. 84-87, Jan. 2016, doi: 10.1038/nature16467.

[2] D. Tilman, C. Balzer, J. Hill, and B. L. Befort, "Global food demand and the sustainable intensification of agriculture," *Proceedings of the National Academy of Sciences,* vol. 108, no. 50, pp. 20260-20264, Dec. 2011, doi: 10.1073/pnas.1116437108.

[3] J. Fanzo, A. L. Bellows, M. L. Spiker, A. L. Thorne-Lyman, and M. W. Bloem, "The importance of food systems and the environment for nutrition," (in eng), *The American Journal of Clinical Nutrition,* vol. 113, no. 1, pp. 7-16, Jan. 2021, doi: 10.1093/ajcn/nqaa313.

[4] R. Gebbers and V. I. Adamchuk, "Precision Agriculture and Food Security," *Science,* vol. 327, no. 5967, pp. 828-831, Feb. 2010, doi: 10.1126/science.1183899.

[5] S. Mitchell, A. Weersink, and N. Bannon, "Adoption barriers for precision agriculture technologies in Canadian crop production," *Canadian Journal of Plant Science,* vol. 101, no. 3, pp. 412-416, June 2020, doi: 10.1139/cjps-2020-0234.

[6] T. Horie, M. Yajima, and H. Nakagawa, "Yield forecasting," *Agricultural Systems,* vol. 40, no. 1, pp. 211-236, Jan. 1992, doi: 10.1016/0308-521X(92)90022-G.

[7] X. Xu *et al.*, "Design of an integrated climatic assessment indicator (ICAI) for wheat production: A case study in Jiangsu Province, China," *Ecological Indicators,* vol. 101, pp. 943-953, June 2019, doi: 10.1016/j.ecolind.2019.01.059.

[8] J. You, X. Li, M. Low, D. Lobell, and S. Ermon, "Deep gaussian process for crop yield prediction based on remote sensing data," in *Proceedings of the AAAI conference on artificial intelligence*, Feb. 2017, vol. 31, no. 1, doi: 10.1609/aaai.v31i1.11172.

[9] C. Toth and G. Jóźków, "Remote sensing platforms and sensors: A survey," *ISPRS Journal of Photogrammetry and Remote Sensing,* vol. 115, pp. 22-36, May 2016, doi: 10.1016/j.isprsjprs.2015.10.004.

[10] R. P. Sishodia, R. L. Ray, and S. K. Singh, "Applications of Remote Sensing in Precision Agriculture: A Review," *Remote Sensing,* vol. 12, no. 19, Sep. 2020, doi: 10.3390/rs12193136.

[11] T. van Klompenburg, A. Kassahun, and C. Catal, "Crop yield prediction using machine learning: A systematic literature review," *Computers and Electronics in Agriculture,* vol. 177, p. 105709, Oct. 2020, doi: 10.1016/j.compag.2020.105709.

[12] L. Deng, Z. Mao, X. Li, Z. Hu, F. Duan, and Y. Yan, "UAV-based multispectral remote sensing for precision agriculture: A comparison between different cameras," *ISPRS Journal of Photogrammetry and Remote Sensing,* vol. 146, pp. 124-136, Dec. 2018, doi: 10.1016/j.isprsjprs.2018.09.008.

[13] T. M. Lillesand, R. W. Kiefer, and J. W. Chipman, *Remote sensing and image interpretation*, Seventh edition. ed. Hoboken, NJ: Wiley (in English), 2015.

[14] J. Xue and B. Su, "Significant Remote Sensing Vegetation Indices: A Review of Developments and Applications," *Journal of Sensors,* vol. 2017, p. 1353691, May 2017, doi: 10.1155/2017/1353691.

[15] J. Liu, J. Xiang, Y. Jin, R. Liu, J. Yan, and L. Wang, "Boost Precision Agriculture with Unmanned Aerial Vehicle Remote Sensing and Edge Intelligence: A Survey," *Remote Sensing,* vol. 13, no. 21, Oct. 2021, doi: 10.3390/rs13214387.

[16] H. Zhang, L. Wang, T. Tian, and J. Yin, "A Review of Unmanned Aerial Vehicle Low-Altitude Remote Sensing (UAV-LARS) Use in Agricultural Monitoring in China," *Remote Sensing,* vol. 13, no. 6, Mar. 2021, doi: 10.3390/rs13061221.

[17] B. Duan *et al.*, "Remote Estimation of Rice Yield With Unmanned Aerial Vehicle (UAV) Data and Spectral Mixture Analysis," *Frontiers in Plant Science,* Methods vol. 10, Feb. 2019, doi: 10.3389/fpls.2019.00204.

[18] D.-W. Kim *et al.*, "Modeling and Testing of Growth Status for Chinese Cabbage and White Radish with UAV-Based RGB Imagery," *Remote Sensing,* vol. 10, no. 4, Mar. 2018, doi: 10.3390/rs10040563.

[19] M. Maimaitijiang, V. Sagan, P. Sidike, S. Hartling, F. Esposito, and F. B. Fritschi, "Soybean yield prediction from UAV using multimodal data fusion and deep learning," *Remote Sensing of Environment,* vol. 237, p. 111599, Feb. 2020, doi: 10.1016/j.rse.2019.111599.

[20] F. J. Mesas-Carrascosa, M. D. Notario García, J. E. Meroño de Larriva, and A. García-Ferrer, "An Analysis of the Influence of Flight Parameters in the Generation of Unmanned Aerial Vehicle (UAV) Orthomosaicks to Survey Archaeological Areas," (in eng), *Sensors (Basel),* vol. 16, no. 11, Nov. 2016, doi: 10.3390/s16111838.

[21] H. Fang and S. Liang, "Leaf area index models," *Encyclopedia of ecology, five-volume set,* 2008, doi: 10.1016/B978-0-12-409548-9.09076-X.

[22] S. Liang and J. Wang, *Advanced remote sensing : terrestrial information extraction and applications*, 2nd ed. London: Academic Press (in English), 2020.

[23] J. W. Rouse, R. H. Haas, J. A. Schell, and D. W. Deering, "Monitoring vegetation systems in the Great Plains with ERTS," *NASA special publication,* vol. 351, no. 1, p. 309, 1974.

[24] C. J. Tucker, "Red and photographic infrared linear combinations for monitoring vegetation," *Remote Sensing of Environment,* vol. 8, no. 2, pp. 127-150, May 1979, doi: 10.1016/0034-4257(79)90013-0.

[25] L. Fan, Y. Gao, H. Brück, and C. Bernhofer, "Investigating the relationship between NDVI and LAI in semi-arid grassland in Inner Mongolia using in-situ measurements," *Theoretical and Applied Climatology,* vol. 95, no. 1, pp. 151-156, Jan. 2009, doi: 10.1007/s00704-007-0369-2.

[26] T. N. Carlson and D. A. Ripley, "On the relation between NDVI, fractional vegetation cover, and leaf area index," *Remote Sensing of Environment,* vol. 62, no. 3, pp. 241-252, Dec. 1997, doi: 10.1016/S0034-4257(97)00104-1.

[27] M. A. Hassan *et al.*, "A rapid monitoring of NDVI across the wheat growth cycle for grain yield prediction using a multi-spectral UAV platform," *Plant Science,* vol. 282, pp. 95-103, May 2019, doi: 10.1016/j.plantsci.2018.10.022.

[28] A. Huete, K. Didan, T. Miura, E. P. Rodriguez, X. Gao, and L. G. Ferreira, "Overview of the radiometric and biophysical performance of the MODIS vegetation indices," *Remote Sensing of Environment,* vol. 83, no. 1, pp. 195-213, Nov. 2002, doi: 10.1016/S0034-4257(02)00096-2.

[29] A. Aklilu Tesfaye and B. Gessesse Awoke, "Evaluation of the saturation property of vegetation indices derived from sentinel-2 in mixed crop-forest ecosystem," *Spatial Information Research,* vol. 29, no. 1, pp. 109-121, Feb. 2021, doi: 10.1007/s41324-020-00339-5.

[30] D. Saravia *et al.*, "Yield Predictions of Four Hybrids of Maize (Zea mays) Using Multispectral Images Obtained from UAV in the Coast of Peru," *Agronomy,* vol. 12, no. 11, Oct. 2022, doi: 10.3390/agronomy12112630.

[31] Y. Liu *et al.*, "A Robust Vegetation Index Based on Different UAV RGB Images to Estimate SPAD Values of Naked Barley Leaves," *Remote Sensing,* vol. 13, no. 4, Feb. 2021, doi: 10.3390/rs13040686.

[32] J. Ansarifar, L. Wang, and S. V. Archontoulis, "An interaction regression model for crop yield prediction," *Scientific Reports,* vol. 11, no. 1, p. 17754, Sep. 2021, doi: 10.1038/s41598-021-97221-7.

[33] G. Freeman, "Statistical methods for the analysis of genotype-environment interactions," *Heredity,* vol. 31, no. 3, pp. 339-354, 1973.

[34] S. Khaki and L. Wang, "Crop yield prediction using deep neural networks," *Frontiers in Plant Science,* vol. 10, p. 621, May 2019, doi: 10.3389/fpls.2019.00621.

[35] A. P. Marques Ramos *et al.*, "A random forest ranking approach to predict yield in maize with uav-based vegetation spectral indices," *Computers and Electronics in Agriculture,* vol. 178, p. 105791, Nov. 2020, doi: 10.1016/j.compag.2020.105791.

[36] S. Shafiee, L. M. Lied, I. Burud, J. A. Dieseth, M. Alsheikh, and M. Lillemo, "Sequential forward selection and support vector regression in comparison to LASSO regression for

spring wheat yield prediction based on UAV imagery," *Computers and Electronics in Agriculture,* vol. 183, p. 106036, Apr. 2021, doi: 10.1016/j.compag.2021.106036.

[37] C. Andreasen, J. Rasmussen, and Z. Bitarafan, "Site-Specific Seed Yield Prediction of Red Fescue (Festuca rubra L.) Based on Drone Imaging and Local Regression Models," *Agronomy,* vol. 13, no. 2, Jan. 2023, doi: 10.3390/agronomy13020316.

[38] S. J. Birrell, K. A. Sudduth, and S. C. Borgelt, "Comparison of sensors and techniques for crop yield mapping," *Computers and Electronics in Agriculture,* vol. 14, no. 2, pp. 215-233, Feb. 1996, doi: 10.1016/0168-1699(95)00049-6.

[39] J. L. Ping and A. Dobermann, "Processing of Yield Map Data," *Precision Agriculture,* vol. 6, no. 2, pp. 193-212, Apr. 2005, doi: 10.1007/s11119-005-1035-2.

[40] A. Schneider, G. Hommel, and M. Blettner, "Linear regression analysis: part 14 of a series on evaluation of scientific publications," (in eng), *Deutsches Ärzteblatt International,* vol. 107, no. 44, pp. 776-82, Nov. 2010, doi: 10.3238/arztebl.2010.0776.

[41] D. C. Montgomery, E. A. Peck, and G. G. Vining, *Introduction to linear regression analysis*. John Wiley & Sons, 2021.

[42] G. E. Box and D. R. Cox, "An analysis of transformations," *Journal of the Royal Statistical Society: Series B (Methodological),* vol. 26, no. 2, pp. 211-243, 1964.

[43] G. Heinze, C. Wallisch, and D. Dunkler, "Variable selection - A review and recommendations for the practicing statistician," (in eng), *Biometrical Journal,* vol. 60, no. 3, pp. 431-449, May 2018, doi: 10.1002/bimj.201700067.

[44] G. Smith, "Step away from stepwise," *Journal of Big Data,* vol. 5, no. 1, p. 32, Sep. 2018, doi: 10.1186/s40537-018-0143-6.

[45] F. E. Harrell, *Regression modeling strategies: with applications to linear models, logistic regression, and survival analysis*. Springer, 2001.

[46] M. Vihinen, "How to evaluate performance of prediction methods? Measures and their interpretation in variation effect analysis," *BMC Genomics,* vol. 13, no. 4, p. S2, June 2012, doi: 10.1186/1471-2164-13-S4-S2.

[47] E. W. Steyerberg *et al.*, "Assessing the performance of prediction models: a framework for traditional and novel measures," (in eng), *Epidemiology,* vol. 21, no. 1, pp. 128-38, Jan. 2010, doi: 10.1097/EDE.0b013e3181c30fb2.

[48] F. K. Martens, J. G. Kers, and A. C. J. Janssens, "External validation is only needed when prediction models are worth it (Letter commenting on: J Clin Epidemiol. 2015; 68: 25-34)," *Journal of Clinical Epidemiology,* vol. 69, pp. 249-250, Feb. 2015, doi: 10.1016/j.jclinepi.2015.01.022.

[49] E. W. Steyerberg, F. E. Harrell, Jr., G. J. Borsboom, M. J. Eijkemans, Y. Vergouwe, and J. D. Habbema, "Internal validation of predictive models: efficiency of some procedures for logistic regression analysis," (in eng), *Journal of Clinical Epidemiology,* vol. 54, no. 8, pp. 774-81, Aug. 2001, doi: 10.1016/s0895-4356(01)00341-9.

[50] D. A. Belsley, E. Kuh, and R. E. Welsch, *Regression diagnostics: Identifying influential data and sources of collinearity*. John Wiley & Sons, 2005.

[51] N. Otsu, "A Threshold Selection Method from Gray-Level Histograms," *IEEE Transactions on Systems, Man, and Cybernetics,* vol. 9, no. 1, pp. 62-66, 1979, doi: 10.1109/TSMC.1979.4310076.

[52] A. A. Gitelson, Y. Gritz, and M. N. Merzlyak, "Relationships between leaf chlorophyll content and spectral reflectance and algorithms for non-destructive chlorophyll

assessment in higher plant leaves," *Journal of Plant Physiology,* vol. 160, no. 3, pp. 271-282, Jan. 2003, doi: 10.1078/0176-1617-00887.

[53] M. Vincini, E. Frazzi, and P. D'Alessio, "A broad-band leaf chlorophyll vegetation index at the canopy scale," *Precision Agriculture,* vol. 9, no. 5, pp. 303-319, Aug. 2008, doi: 10.1007/s11119-008-9075-z.

[54] T. Kataoka, T. Kaneko, H. Okamoto, and S. Hata, "Crop growth estimation system using machine vision," in *Proceedings 2003 IEEE/ASME International Conference on Advanced Intelligent Mechatronics (AIM 2003)*, Sep. 2003, vol. 2: IEEE, pp. b1079-b1083 vol. 2, doi: 10.1109/AIM.2003.1225492.

[55] D. M. Woebbecke, G. E. Meyer, K. Von Bargen, and D. A. Mortensen, "Color indices for weed identification under various soil, residue, and lighting conditions," *Transactions of the ASAE,* vol. 38, no. 1, pp. 259-269, 1995, doi: 10.13031/2013.27838.

[56] M. Louhaichi, M. M. Borman, and D. E. Johnson, "Spatially Located Platform and Aerial Photography for Documentation of Grazing Impacts on Wheat," *Geocarto International,* vol. 16, no. 1, pp. 65-70, Mar. 2001, doi: 10.1080/10106040108542184.

[57] A. A. Gitelson, Y. J. Kaufman, and M. N. Merzlyak, "Use of a green channel in remote sensing of global vegetation from EOS-MODIS," *Remote Sensing of Environment,* vol. 58, no. 3, pp. 289-298, Dec. 1996, doi: 10.1016/S0034-4257(96)00072-7.

[58] J. Bendig *et al.*, "Combining UAV-based plant height from crop surface models, visible, and near infrared vegetation indices for biomass monitoring in barley," *International Journal of Applied Earth Observation and Geoinformation,* vol. 39, pp. 79-87, July 2015, doi: 10.1016/j.jag.2015.02.012.

[59] N. S. Goel and W. Qin, "Influences of canopy architecture on relationships between various vegetation indices and LAI and Fpar: A computer simulation," *Remote Sensing Reviews,* vol. 10, no. 4, pp. 309-347, Dec. 1994, doi: 10.1080/02757259409532252.

[60] G. Rondeaux, M. Steven, and F. Baret, "Optimization of soil-adjusted vegetation indices," *Remote Sensing of Environment,* vol. 55, no. 2, pp. 95-107, Feb. 1996, doi: 10.1016/0034-4257(95)00186-7.

[61] R. D. Cook, "Influential observations in linear regression," *Journal of the American Statistical Association,* vol. 74, no. 365, pp. 169-174, 1979.

[62] A. Milioto, P. Lottes, and C. Stachniss, "Real-Time Semantic Segmentation of Crop and Weed for Precision Agriculture Robots Leveraging Background Knowledge in CNNs," in *2018 IEEE International Conference on Robotics and Automation (ICRA)*, May 2018, pp. 2229-2235, doi: 10.1109/ICRA.2018.8460962.

[63] E. H. Land, "The retinex theory of color vision," (in eng), *Scientific American,* vol. 237, no. 6, pp. 108-28, Dec. 1977, doi: 10.1038/scientificamerican1277-108.

[64] E. H. Land and J. J. McCann, "Lightness and retinex theory," (in eng), *Journal of the Optical Society of America,* vol. 61, no. 1, pp. 1-11, Jan. 1971, doi: 10.1364/josa.61.000001.

[65] S. M. Pizer *et al.*, "Adaptive histogram equalization and its variations," *Computer Vision, Graphics, and Image Processing,* vol. 39, no. 3, pp. 355-368, Sep. 1987, doi: 10.1016/S0734-189X(87)80186-X.

[66] S. Rahman, M. M. Rahman, M. Abdullah-Al-Wadud, G. D. Al-Quaderi, and M. Shoyaib, "An adaptive gamma correction for image enhancement," *EURASIP Journal on Image*

and Video Processing, vol. 2016, no. 1, p. 35, Dec. 2016, doi: 10.1186/s13640-016-0138-1.

[67] S. Ors and D. L. Suarez, "Spinach biomass yield and physiological response to interactive salinity and water stress," *Agricultural Water Management,* vol. 190, pp. 31-41, Aug. 2017, doi: 10.1016/j.agwat.2017.05.003.

[68] J. Gillberg, P. Marttinen, H. Mamitsuka, and S. Kaski, "Modelling G×E with historical weather information improves genomic prediction in new environments," *Bioinformatics,* vol. 35, no. 20, pp. 4045-4052, Oct. 2019, doi: 10.1093/bioinformatics/btz197.

[69] D. Ekaso, F. Nex, and N. Kerle, "Accuracy assessment of real-time kinematics (RTK) measurements on unmanned aerial vehicles (UAV) for direct geo-referencing," *Geo-Spatial Information Science,* vol. 23, no. 2, pp. 165-181, Jan. 2020, doi: 10.1080/10095020.2019.1710437.

[70] C. Ballester, J. Hornbuckle, J. Brinkhoff, J. Smith, and W. Quayle, "Assessment of In-Season Cotton Nitrogen Status and Lint Yield Prediction from Unmanned Aerial System Imagery," *Remote Sensing,* vol. 9, no. 11, Nov. 2017, doi: 10.3390/rs9111149.

[71] T. B. Raper and J. J. Varco, "Canopy-scale wavelength and vegetative index sensitivities to cotton growth parameters and nitrogen status," *Precision Agriculture,* vol. 16, no. 1, pp. 62-76, Feb. 2015, doi: 10.1007/s11119-014-9383-4.

[72] H. Sheng, X. Chen, J. Su, R. Rajagopal, and A. Ng, "Effective data fusion with generalized vegetation index: Evidence from land cover segmentation in agriculture," in *Proceedings of the IEEE/CVF Conference on Computer Vision and Pattern Recognition Workshops*, July 2020, pp. 60-61, doi: 10.1109/CVPRW50498.2020.00038.

[73] J. Das *et al.*, "Devices, systems, and methods for automated monitoring enabling precision agriculture," in *2015 IEEE International Conference on Automation Science and Engineering (CASE)*, Aug. 2015, pp. 462-469, doi: 10.1109/CoASE.2015.7294123.

[74] S. Shorewala, A. Ashfaque, R. Sidharth, and U. Verma, "Weed Density and Distribution Estimation for Precision Agriculture Using Semi-Supervised Learning," *IEEE Access,* vol. 9, pp. 27971-27986, Nov. 2021, doi: 10.1109/ACCESS.2021.3057912.

[75] M. T. Chiu *et al.*, "Agriculture-vision: A large aerial image database for agricultural pattern analysis," in *Proceedings of the IEEE/CVF Conference on Computer Vision and Pattern Recognition*, Aug. 2020, pp. 2828-2838, doi: 10.1109/CVPR42600.2020.00290.

[76] M. Louargant *et al.*, "Unsupervised Classification Algorithm for Early Weed Detection in Row-Crops by Combining Spatial and Spectral Information," *Remote Sensing,* vol. 10, no. 5, May 2018, doi: 10.3390/rs10050761.